End plate gap effects on a half-wing model.

by

Subrahmanyam Kuppa

Thesis submitted to the Faculty of the
Virginia Polytechnic Institute and State University
in partial fulfillment of the requirements for the degree of
Master of Science
in
Aerospace Engineering

APPROVED:

Dr.J.F. Marchman III, Chairman

Dr.J.A. Schetz

Dr.W.L. Neu

April, 1987

Blacksburg, Virginia

End plate gap effects on a half-wing model.

by

Subrahmanyam Kuppa
Dr.J.F. Marchman III, Chairman
Aerospace Engineering

(ABSTRACT)

Differences in the aerodynamic performance data obtained at different test facilities were observed for the Wortmann FX-63-137 airfoil. Earlier investigations found that the size of the hysteresis loop was affected by the tunnel environment and that single strut mounting of a three dimensional wing model interfered negligibly with the wing. Theoretical and experimental evaluations of a half wing model mounted with an end plate gap were done. Vortex panel method was used in the theoretical evaluation. The results from this indicated an effect of reduced aspect ratio with increase in end plate gap size.

Tests were conducted in the VPI Stability Tunnel at low Reynolds numbers for different gap sizes including sealed gap. Results from the experiments showed that even very small gaps produce substantial changes in zero lift angle of attack (α_{L0}) and the change in α_{L0} was reduced as Reynolds number increased. Sealed gap test results did not show such a behaviour. Flow visualization of the flow through the gap showed a significant flow through the gap even at very low Reynolds number and small gap size.

Acknowledgements

I sincerely wish to thank Dr. Marchman for the advice and encouragement provided during the course of this study. I also wish to thank Dr. J.A. Schetz and Dr. W.L.Neu for serving on my committee.

Thanks are due to for his help in setting up the experiments.

I would also like to thank my parents for their love and support.

Finally, I thank my friends for all their help and encouragement.

Table of Contents

List of Illustrations

NOMENCLATURE

A	Influence coefficient
AR	Wing aspect ratio
C_A	Axial force coefficient
C_D	Drag coefficient
C_{D_i}	Induced drag coefficient
C_{D_0}	Drag coefficient at zero lift
C_L	Lift coefficient
C_N	Normal force coefficient
C_p	Pressure coefficient
DEL	Gap size at the end plate for computation
G	Strength of vortex loop
$\vec{i}$	Unit vector in the direction of X-axis
$\vec{j}$	Unit vector in the direction of Y-axis
$\vec{k}$	Unit vector in the direction of Z-axis
$\vec{n}$	Unit normal vector
P	Static pressure
P_t	Total pressure

q	Dynamic pressure
Re	Reynolds number
U	Free stream velocity
$\vec{V}$	Velocity
W	Aircraft weight
X	Axis along the wing center line
Y	Axis perpendicular to X-axis in wing plane
Z	Axis normal to X and Y
α	Wing angle of attack
$\vec{\gamma}$	Strength of vortex sheet
$\vec{\Gamma}$	Strength of vortex filament
μ	Coefficient of viscosity ; Doublet Strength
ρ	Air density
σ	Source strength
φ	Perturbation velocity potential
Φ	Total velocity potential
$\vec{\omega}$	Vorticity

I. Introduction

In recent years much research has been devoted to the study of wing aerodynamics at low Reynolds numbers. Most of this work has been prompted by the desire of the United States Navy to design Remotely Piloted Vehicles (RPVs) capable of cruise at ship speed at very low altitudes. Conventionally, the wing chord length is used as the characteristic length in wing and aircraft aerodynamics, and any flow situation where the Reynolds number falls below 500,000 is termed low Reynolds number regime. For an aircraft in level flight, the definitions of the Reynolds number and the lift coefficient yield the relationship,

$$Re = \sqrt{\frac{2\,W}{C_L}\,\frac{1}{AR}\,\frac{\rho}{\mu^2}} \tag{1.1}$$

where μ is the viscosity of air, W is the weight of the vehicle and AR, the aspect ratio of the wing. Hence, low Reynolds number situations will be encountered for flight at high altitude, low velocity or small reference lengths. Typically, low Reynolds numbers occur in applications of High-Altitude Aircraft Platforms

(HAAPs), sailplanes, ultralight aircraft, wind turbines and inboard sections of helicopter rotor blades.

Airfoil sections that have been successfully used at high Reynolds numbers possess many inherent deficiences for use at Reynolds numbers less than 500,000. In addition, Lissaman (1983) has noted that below a typical Reynolds number of about 70,000, the airfoil section fails to behave like an airfoil. These decreases in performance are mainly due to relatively large viscous effects leading to premature flow separation.

Certain peculiar flow phenomena are observed at low Reynolds numbers over airfoils. The 'separation bubble' is one of these. It is a local region of separated flow over the airfoil surface. The laminar boundary layer separates from the airfoil surface and the flow reattaches further downstream as a turbulent boundary layer. The effect of this bubble on the flow over the upper surface can be localized or extend over the entire upper surface depending on the conditions. The occurrence of the bubble leads to the phenomenon of 'stall hysteresis'.

The phenomenon of 'stall hysteresis' is presented here in figure 1 from reference 1. In this figure, an aspect ratio 8 wing appears to go through a normal increase in lift coefficient as angle of attack is increased and through the stall at $C_{L\max}$. However, when the angle of attack after stall is decreased, the wing does not retrace its prestall behaviour. Instead, the lift drop remains and the curve returns to the prestall value only after a considerable reduction in angle of attack. Thus, a loop is produced. This can lead to severe problems in stall recovery. This behaviour becomes very important when considering design of low Reynolds number vehicles. For a RPV operating at an altitude of 50 feet, should stall occur upon encountering a gust, the recovery should be immediate to avoid any significant loss in altitude. Hence, careful experimental and theoretical evaluation of the aerodynamic performance of airfoils and wings at low Reynolds numbers is essential for the data generated to be useful to the designer. Mueller (1985) stresses the importance of the sensitivity of the behaviour of the boundary layer on the airfoil to disturbances like turbulence and roughness.

Apart from these disturbances model testing techniques also seem to influence the results. Much data has been generated in different facilities at low Reynolds numbers for the Wortmann FX-63-137 airfoil (figure 2). Render (1985), Mueller (1985) and Liebeck and Camacho (1985) have published results for two dimensional models of the Wortmann airfoil. Miley (1982) presented a catalog of low Reynolds number airfoil data for wind turbines. For finite wings only Mueller (1985), Bastedo and Mueller(1985) at the University of Notre Dame (Notre Dame), Abtahi and Marchman(1985), Marchman, Abtahi, Sumantran and Sun (1985), Marchman, Sumantran and Schaefer(1985) and Sun, Sumantran and Marchman(1985) at Virginia Tech have published data which show the existence of the hysteresis loop. An aspect ratio of 8.9 has been dealt with, by Render (1985) at Cranfield, but the data failed to record the sensitive hysteresis loop. The aspect ratios dealt with at Notre Dame are 3,4 and 5.6, and at Virginia Tech are

4,6,8 and 10. Though the data show good agreement in the values for the lift curve slopes and $C_{L\,\max}$, some differences exist among them.

Most of the concern is about the data published by the researchers at Notre Dame and Virginia Tech, the first U.S. facilities to obtain finite wing aerodynamic performance data for the Wortmann airfoil. The data obtained at Notre Dame shows significant shift in the zero lift angle of attack as compared to the Virginia Tech data. The test methods used at Virginia Tech and Notre dame are different. Hence, some differences in the test data is to be expected. Since experience in low Reynolds number testing of wings is limited, it is difficult to establish the causes for the differences among the data obtained with different test methods.

The differences in test data from different facilities poses the problem of reliability of the test methods at low Reynolds numbers. Due to the occurrence of the stall hysteresis loop phenomenon, the angles of attack at stall and stall recovery become very important parameters while considering design of low Reynolds number vehicles. Therefore, it becomes necessary to evaluate the performance of different test methods as they give different results.

Some investigation has already been done regarding the test method used at Virginia Tech by Marchman and Sumantran (1985). They investigated a possible shift of the zero angle of attack due to interference of the strut mounting used in the experiments to generate data for finite wings. After exhaustive tests it was concluded that their set-up was not causing a shift in zero lift angle of attack (α_{L0}) Thus, it becomes necessary to evaluate the test method used at Notre Dame, where a semi-span wing model was set-up with an end-plate gap for testing. There is immense likelyhood of contamination of the flow on the wing due to the interaction of the boundary layers at the junction of the wing model and end-plate. Apart from such interaction, a leakage from the windward surface to the leeward surface of the wing can cause further contamination of the flow on the wing. With such an alteration of the flow field in the presence of an end-plate, discrepancies in the data should be expected. However, the specific differences in data that should be expected remain to be established. Very little is known about testing semi-span wing models with end-plate gaps at low Reynolds numbers.

The current research program was formulated with the major objective of finding the effect of the gap on the lift and drag of a semi-span wing. The emphasis was on obtaining force data for the model subjected to different gap sizes and different Reynolds numbers. The present study involved :

1. Computational evaluation of the effect of the gap with an ideal fluid flow assumption.

2. Experimental study of the effect of the end-plate gap by obtaining force data from the strain gauge strut in the Stability Wind Tunnel of Virginia Tech.

3. Flow visualization of the flow through the gap using surface-oil flow technique.

II. Effects of Different Test Techniques

The differences in data from different facilities will be examined in the following sections of this chapter. A review of the problems associated with different low speed test techniques is essential, before examining the differences. The different test data will then be compared in the light of these problems. Further, effects of semi- span testing with end plate gap will also be examined, as it is relevant to the present study.

2.1 Differences in Low Speed Test Methods

There are different ways of mounting a wing model in the wind tunnel for testing at low speeds. Depending upon the size of the test section, size of the wing model, objective of the test, convenience, etc., it will be necessary to select a method of mounting the model. A wing model can be mounted on

1. a single strut (fig.3), or
2. a sting (fig.4), or
3. a short strut using a half model (fig.5).

Results obtained by each of these methods may not agree with each other, as the interference effects are different in each case. In particular, low Reynolds number data from Virginia Tech and Notre Dame do not agree with each other. A single strut mounting arrangement was used at Virginia Tech, while a half model with an end plate was used at Notre Dame. The arrangement at Notre Dame had a gap between end plate and the wing. Some data was generated at Cranfield using the half model mounting, but with the end plate attached to the wing. No results are yet available with a sting mount arrangement for the low Reynolds number range.

Single strut mounting is the simplest arrangement. The three dimensional wing model is mounted on a strut. Only one shroud is necessary to shelter the strut so that there is no contamination of the force data due to the strut. The shroud need not move as the model is rotated in yaw. Usually full vehicle models on a single strut will need strong support and hence the size of the strut near attachment will be large. However, when only a wing model is considered the size can be smaller than needed for a big, full vehicle model. When the size of the strut at the attachment point is large, the interference is considerable. Even when the size is small, there is some interference at the strut attachment under the wing. This interference is pronounced if the shroud fairing is too close to the model. This can cause local flow angularity causing an error in the angle of attack. Also, when the shroud cross-sectional area perpendicular to the flow is comparable to that of the wind-tunnel, then blockage effects due to the shroud need to be accounted.

Mounting a half model on a short strut with an end plate gap has the advantage of a decrease in total drag of the set-up. The other advantages over full model testing are as follows :

- Half models are cheaper and easier to manufacture as compared to a full model due to easier experiment control and rigging.

- A static balance or an oscillatory test rig can be placed outside the tunnel, resulting in a simpler and more efficient design as compared to internal balances and test rigs.

- Pressure measurements on parts away from the plane of symmetry can be done easily.

- For a given tunnel (i.e. size and dynamic pressure fixed), a larger characteristic length can be used with a half model than with a full model. Hence, a larger Reynolds number can be obtained.

Inspite of all these advantages, some effects limit the reliability of test results obtained by mounting half models. This type of mounting introduces a lot of interference effects. These effects are mainly due to the end plate boundary layer and the gap between the end plate and the wing. Pope (1966) mentions that if the gap is kept small enough, its effect will probably be negligible. However, he warns strongly of the adverse effects on the results if the gap is not kept small enough. He says that inviscid considerations indicate that a gap of 0.001 times the full span of the wing will decrease the effective aspect ratio enough to increase the induced drag by 31 percent; a gap of 0.01 span will cause an increase of 47 percent. He mentions that the effect of viscosity will tend to decrease the error, but the degree of viscous effect has not been clearly understood. He also states that it is often difficult to decide on a small enough gap.

Attaching the half wing model to an end plate, as done at Cranfield has the same problems of boundary layer interference near the root as discussed before. In addition, the drag of the plate is to be subtracted to get the final result. This subtraction is of considerable importance in low Reynolds number testing as the lift and drag forces involved are small due to the low dynamic pressure and small size of the model.

Sting mounting of a model is attractive if the model can be mounted without affecting its geometry. However, it is usually necessary to strengthen the model at the point of attachment to the sting. This may introduce some modification of the geometry of the wing model. When such modification is done, the reliability of the test results is again in question. If it is possible to mount a wing without any modification that would alter the flow on the model, it would be worthwhile to pursue this type of mounting with a three dimensional wing model. Also, at high angles of attack the vortices shed from the sting support can alter the flow on the wing. If the sting is slender enough near the attachment, then the vortices shed from it may not be strong enough to cause any flow variation on the wing. The sting can be made slender enough, as the aerodynamic loads encountered on a small model at low speeds are small as compared to high speed testing, where a sting support is usually employed.

2.2 *Differences in Test data*

The differences in test data from Notre Dame and Virginia Tech can be summarized as follows :

1. Notre Dame results show a Reynolds number effect. The linear portion of the $C_L - \alpha$ curve shifts to the left as Reynolds number increases (see figure 6). Neither the Cranfield study nor the Virginia Tech results show such a shift with Re.

2. Virginia Tech and Notre Dame data for similar aspect ratio wings at the same Reynolds numbers show good agreement except for a shift in the zero lift angle.

3. Notre Dame data shows much smaller sized hysteresis loops as compared to the Virginia Tech data.

4. The Cranfield data compares well with the Virginia Tech data in the zero lift angle of attack but shows a significantly higher lift curve slope.

Since a bulk of the data originated from the work done at Virginia Tech and Notre Dame , the dispute in results is chiefly among them.

The question of the size of the hysteresis loop can be answered in terms of the acoustic and turbulence level of the tunnel environment. As reported by Marchman, Sumantran and Schaefer (1985), both acoustic and turbulence levels can cause a change in the size of the hysteresis loop. Their results showed (figs.7 and 8) that increases in turbulence can substantially reduce the stall hysteresis effect and can even eliminate the loop. Acoustic disturbances of the proper frequency and level can produce similar effects. However, neither of them were observed to produce any shift of the zero lift angle of attack.

The shift in zero lift angle of attack is similar to that caused by a change in camber. This indicates that there may be a loss of lift due to separation on the surface. The Wortmann airfoil is designed to operate at near separation on the lower surface . Therefore any disturbance of the flow on the lower surface would result in flow separation and hence a loss of lift. The difference in zero lift angle of attack in Notre Dame and Virginia Tech results may be due to such a separation.

Reynolds number changes are not known to alter the linear portion of the lift curve. They are only known to influence a wing's stall behaviour. For example, consider the $C_L - \alpha$ curves obtained by Althaus at Stuttgart, in figure 9. These curves present the results at Reynolds numbers of 150,000 and 230,000. These results clearly show that the $C_L - \alpha$ curves do not shift with Reynolds number. This influence seen in the Notre Dame results were attributed to change in the size of the laminar separation bubble as Reynolds number changes. At low angles of attack the influence of the bubble is relatively small. Figure 10 from ref.10 shows the effect of Reynolds numbers of 100,000 , 150,000 and 200,000 on the airfoil pressure distribution. It is seen that as Reynolds number increases, the size of the bubble decreases, a change which should decrease the lift rather than increase it. Therefore, a shift of the $C_L - \alpha$ curve to the right rather than left is to be expected. However, the change in the area of the pressure curve is rather small to produce any appreciable change in C_L with increase in Reynolds number at low angles of attack.

As already noted, there are major differences in the test techniques employed at Notre Dame and Virginia Tech. The strut mount arrangement used at Virginia Tech was found to give the correct value for C_L and zero angle of attack for a flat plate wing of aspect ratio 6, similar in planform to a Wortmann wing of the same aspect ratio. The $C_L - \alpha$ curve obtained is as in fig.11 from reference 10. This indicates that there is no flow angle effect due to the strut in the tunnel test section. Marchman and Sumantran (1985) reported that further tests with inverted models and image struts gave no further reason to suspect that strut interference had influenced the data taken at Virginia Tech.

Research workers at Cranfield (Dyer and Stollery (1986)) compared the performance of the Wortmann FX-63-137 airfoil to other airfoils for application to RPVs. In the process of evaluation they used both theoretical and experimental results. The theoretical results were obtained by the method due to Williams(1984). He used a viscous-inviscid interaction method to predict lift and drag, and movement of the position of transition from laminar to a turbulent boundary layer with increasing angle of attack. The theoretical pressure distributions obtained at incidences of 8° and 16° have been compared to those obtained by experiment. These results are presented here in figures 15a and 15b, as reported by Dyer and Stollery(1986). At an incidence of 16° the flow is separated, but at 8° it is attached. However, the theory and experiment agree very well. Figure 14 shows the $C_L - \alpha$ curve obtained at Cranfield at a Reynolds number of 3×10^5. This figure indicates a zero lift angle of attack of about $-8°$, which is close to the value of $-8.5°$ observed in the results of Virginia Tech. Also, Althaus′ results in figure 9, when extrapolated, give the same value of the zero lift angle of attack.

Mueller et al. (1986) recently reported results from experiments conducted to evaluate the effect of the end-plate gap on the lift and drag coefficients. They reported lift and drag curves for different gap widths at a Reynolds number of 150,000. Their results are presented here in figures 12 and 13. As is evident, these curves do not show any variation with gap size. The figures show results for the case when the gap was filled with petroleum jelly. Even in this case the curves do not show any shift. Mueller and his associates, however, did not report the effectiveness of the petroleum jelly used to seal the gap in their experiments. The Wortmann FX-63-137 ESM section, figure 2, is quite thin at and near the trailing edge. It is unlikely that the gap would be properly sealed with petroleum jelly over the entire section, especially at the centre and the trailing edge, when the angle of attack is high. When the sealing is not intact or is improper, then it is likely that it will not make a difference in results, as the flow near the trailing edge is very sensitive and important for the Wortmann airfoil. This could be the reason for not observing a shift in the lift coefficient curves by Mueller and his associates.

Some preliminary tests were performed at Virginia Tech with a half span model with an end plate, similar to the set-up used at Notre Dame. Figure 16 from reference 10 compares the results obtained with a gap, with those obtained with the gap sealed and the Notre Dame results. A model of effective aspect ratio of 4 was used. The data produced with a gap matches the behaviour reported by Notre Dame with the gap open and matches the Virginia Tech strut mounted results with the gap sealed. This confirms that the gap between the wing model and plate can reduce the lift to such as to cause an effective shift in the lift curve.

Almost all the discussion in this section is devoted to the differences in the results with respect to lift coefficient data. At low speeds lift data is usually more reliable than drag data. This is due to the fact that the forces measured in low speed tests are very small. Moreover, drag forces are smaller than lift forces by an order of magnitude. Yet, drag data was obtained reliably at Virginia Tech for Reynolds numbers greater than 80,000. A comparison of drag data (Marchman and Sumantran (1985)) showed that drag measured at Virginia Tech on a strut mounted wing was generally less than that measured at Notre Dame. If there was any interference due to the strut, an increase in drag would be expected. The different test methods involved in producing the data are susceptible to errors due to strut interference (Virginia Tech) or inability to properly account for wing/plate interaction (Notre Dame and Cranfield).

2.3 *Effects of the End-plate Gap on a Half-wing*

The use of half models introduces a number of interference effects, which limit the reliability of test results.The effects are mainly due to (from references (19) & (24)).

- Subsonic downwash interference,
- End-plate boundary layer,

- A gap between model and end-plate.

The model used in preliminary half-span tests at Virginia Tech measures ten inches along the span with a five inch chord, while the wind tunnel test section is 23 feet long with a 6′x6′ cross-section. Also, the model was mounted approximately at the centre of the test section cross section. Considering the relatively small size of the model as compared to the test section, downwash interference effects are negligible as also the corrections thereof. Hence, these effects are not considered in the present discussion.

The boundary layer on the end-plate has a considerable effect on the flow over the wing model near the junction of the model and the plate. Galbraith (1985), made some observations regarding the corner flow at the junction of the airfoil and the end plate, while studying the characteristics of a GU25-5(11)8 airfoil. He observed the oil flow pattern at the wall-airfoil junction (see fig.17). It was seen that the corner boundary layer separates before the main airfoil separation bubble, at which the corner flow is enhanced and results in a strong standing vortex. The effect of this is to decrease the lift on the model close to the plate. Furthermore, the trailing vortices resulting from such a change in lift would have an effect on the total lift distribution on the model.

The gap between the model and the end-plate is introduced by the method of mounting. In many practical half-model rigs, a small leak exists at the model root, so that when the model is at an incidence a flow occurs from the windward surface to the leeward surface. This can cause early separation on the leeward surface, near the model root. When the span of the model is small, the area in which the separation occurs on the upper surface is a considerable fraction of the total area of the semi-span wing.. Thus, the lift producing area is reduced to a fraction of the actual area of the model. That is, there is loss in lift as compared to the model without such separation as mentioned.

An attempt has been made to study further, the effects of the end plate gap at different Reynolds numbers. First, the effect of gap on the $C_L - \alpha$ curve of a rectangular wing in inviscid flow was studied using the vortex lattice technique. Then tests were conducted with different gap sizes and through a Reynolds number range, using a semi span model of aspect ratio 2 (effective AR of 4). In the following chapters, the analytical formulation, experimental set-up and the results obtained from both are dealt with, in detail.

III. Analytical Consideration

An attempt has been made to evaluate the effect of a gap at the root on the lift of a rectangular wing using the vortex lattice method and then look at the experimental results in the light of those results. Pope (1966) in his autoritative text on wind tunnel testing, mentions theoretical considerations of the end plate gap problem, but provides no reference. He states that a gap will decrease the effective aspect ratio. This result was confirmed by the analysis described in the following sections.

The half span wing with the end plate can be modeled as a full span wing with the vertical plane at the root of the wing as the plane of reflection. When the gap is present, then too, the reflection plane model can be used, with the gap also being reflected. The following sections of this chapter discuss the basic principle used in the analysis, formulation of the problem for computation, solution and calculation of aerodynamic loads.

3.1 Basic Principle

For an incompressible flow over a solid body, the continuity equation for the flow field is,

$$\nabla \cdot \vec{V} = 0 \tag{3.1}$$

If the flow is also irrotational, there exists a scalar function Φ (x,y,z) which has a gradient equal to the velocity at each field point in the flow field such that $\vec{V} = \nabla\Phi$. Then the continuity equation becomes the governing Laplace equation,

$$\nabla^2\Phi = 0 \tag{3.2}$$

The boundary conditions for this case can be written as,

$$\nabla\Phi = \vec{V}_\infty \qquad at \quad \infty$$

$$\nabla\Phi \cdot \vec{n} = 0 \qquad on\ body\ surface \tag{3.3}$$

where $\vec{V}_\infty$ = free stream velocity and $\vec{n}$ = unit normal vector on the body surface.

Without a solid body in the flow field, the solution of the equation (3.2) becomes $\Phi = V_\infty x$, if an axes system is chosen such that $\vec{V}_\infty$ is parallel to the X-axis.

Separating the free stream solution $\varphi_\infty = V_\infty x$ from the influence of a solid body, the velocity potential can be written as,

$$\Phi = \varphi_\infty + \varphi \tag{3.4}$$

where φ is the perturbation velocity potential due to the presence of a solid body in the flow field. This superposition is possible because the governing equation (3.2) is a linear differential equation. Since φ_∞ is known, rewriting the governing equation w.r.t. φ alone,

$$\nabla^2 \varphi = 0 \tag{3.5}$$

with the boundary conditions,

$$\varphi = 0 \qquad \textit{and}$$

$$\nabla \varphi = 0 \qquad \textit{at} \quad \infty$$

$$\begin{aligned} \nabla \Phi \cdot \vec{n} &= \nabla(\varphi_\infty + \varphi) \cdot \vec{n} \\ &= 0 \qquad \textit{on body surface.} \end{aligned} \tag{3.6}$$

To find the solution for the Laplace equation, one starts from the divergence theorem. For any continuous vector field A, in a domain D enclosed by the body surface S and outer boundary Σ which is located at an infinite distance from the body, the divergence theorem can be written as,

$$\iiint_D \nabla \cdot \vec{A}\, dD = \iint_{S+\Sigma} \vec{A} \cdot \vec{n}\, dS \tag{3.7}$$

Let

$$A = \psi \nabla \psi' \tag{3.8}$$

Then Green's second theorem is obtained by substituting for A in equation (3.7),

$$\iiint_D [\psi \nabla^2 \psi' - \psi' \nabla^2 \psi]\, dD = \iint_{S + \Sigma} [\psi \frac{\partial \psi'}{\partial n} - \psi' \frac{\partial \psi}{\partial n}]\, dS \tag{3.9}$$

The solution for the Laplace equation (3.5) can be obtained, if the proper function ψ' in equation (3.9) is found. For this purpose, introduce the singularity functions that have a picking-out property. They are $1/r$ for the three-dimensional problem and ln(r) for the two-dimensional problem, where r is the distance of any point from a fixed point P(x,y,z), where both points are in the same domain D. The singularity function is harmonic except at $r = 0$ and can be expressed as,

$$\nabla^2 (\frac{1}{r}) = - 4\pi \delta(r) \tag{3.10}$$

where $\delta(r)$ is the Dirac delta function. Substituting φ and $1/r$ for ψ and ψ' respectively in equation (3. 9), the integration over the outer boundary Σ will yield zero because of the boundary conditions (3.6) at infinity. Equation (3. 9) becomes,

$$\varphi(P,t) = - \frac{1}{4\pi} \iint_S \frac{1}{r} \frac{\partial \varphi}{\partial n}\, dS + \frac{1}{4\pi} \iint_S \varphi \frac{\partial}{\partial n} (\frac{1}{r})\, dS \tag{3.11}$$

where P = P(x,y,z). This gives the value of φ at any point P in the flow field in terms of the value of φ and $\frac{\partial\varphi}{\partial n}$ at the boundary. The first term in equation (3.11) has the same form as the velocity potential due to the source distributed on the body surface with source density $\frac{\partial\varphi}{\partial n}$ per unit area. The second term is the same as the velocity potential due to the surface distribution of the doublet with doublet density φ. Replacing $\frac{\partial\varphi}{\partial n}$ and φ with source density σ and doublet density μ, equation (3.11) becomes,

$$\varphi = \iint_S \sigma\left(\frac{-1}{4\pi r}\right)dS + \iint_S \mu\frac{\partial}{\partial n}\left(\frac{1}{4\pi r}\right) dS \qquad (3.12)$$

where, $\varphi = \varphi$ (P,t) velocity potential

$\sigma = \sigma$ (Q,t) source density

$\mu = \mu$ (Q,t) doublet density

P : point in flow field D

Q : point on the body surface S

r : distance between P and Q

n : normal to S at Q, positive into the flow,
doublet axis direction is normal to S

There exists an infinite number of σ (Q,t) and μ (Q,t) distributions producing the same solution in flow field D, but they will produce different solutions on surface S. The key is to find σ (Q,t) and μ (Q,t) that yields a solution satisfying the boundary conditions.

Generally, source distributions provide the shape of the body and doublet distributions provide load characteristics. Since solutions for lift are desired, only the doublet distributions will be considered. Then equation (3.12) becomes,

$$\varphi = \iint_S \mu \frac{\partial}{\partial n}\left(\frac{1}{4\pi r}\right) dS \tag{3.13}$$

Since the boundary conditions enforce zero normal velocity on the body surface (Neumann type B.C.), the solution φ can be obtained uniquely with the difference in additive constant. Hence, if the solution is found in terms of velocity, then it will be unique since the velocity is the gradient of the velocity potential. The boundary condition (3.6) at an arbitrary point on the body surface can be written as,

$$-\vec{V}_{\infty n} = \nabla\varphi \cdot \vec{n} \tag{3.14}$$

where $\vec{V}_{\infty_n} = \nabla\varphi_\infty \cdot \vec{n}$.

Since φ is defined in D,

$$\begin{aligned} -\vec{V}_{\infty n} &= \nabla_Q \varphi \cdot \vec{n}_Q \\ &= \lim_{P \to Q}(\nabla_P \varphi \cdot \vec{n}_P) \end{aligned} \tag{3.15}$$

where the subscripts P and Q refer the points where the gradient is evaluated. Substituting equation (3.13) in equation (3.15),

$$-\vec{V}_{\infty n}=\lim_{P\to Q}\left\{\iint_S \mu(Q)\ \vec{n}_P\cdot\nabla_P\left[\frac{\partial}{\partial n}\left(\frac{1}{4\pi r}\right)\right]dS\right\} \qquad (3.16)$$

the above equation can be abbreviated as,

$$-\vec{V}_{\infty n}=\iint_S \mu(Q)\ \vec{n}_Q\cdot\vec{V}_\mu(P;Q)\ dS \qquad (3.17)$$

where $\vec{V}_\mu(P;Q)$ is the induced velocity at P by a doublet of unit strength at Q. The governing equation (3.5) with boundary conditions (3.6) is changed to the integral equation (3.17).

Dividing the body surface S into an infinite number of small surface elements, equation (3.17) becomes,

$$-\vec{V}_{\infty n i}=\sum_{i=1}^{\infty}\sum_{j=1}^{\infty}\mu_j A_{ij} \qquad (3.18)$$

where $\vec{V}_{\infty_{ni}}$: normal component of free stream velocity at i-th surface element

μ_j : doublet strength of j-th surface element

A_{ij} : normal component of induced velocity at i-th surface element by a unit strength doublet at j-th surface element

An approximate solution to the above equation can be obtained by dividing the surface into a finite number of surface elements. If the surface is divided into M panels, then equation (3.18) is applied at only M discrete points on the surface, which are usually called control points. Then equation (3.18) becomes,

$$[A]\{\mu\} = \{R\} \tag{3.19}$$

A_{ij} is the normal component of the induced velocity at the i-th control point by a doublet of unit strength at the j-th panel. R_i is the normal component of free stream velocity at i-th surface element ($-V_{\infty_{n i}}$) and μ_j is the doublet strength of j-th surface element. They are functions of geometry and are calculated before solving for μ 's. After μ 's are obtained, all other desired flow properties can be calculated using the discrete form of equation (3.13).

A surface doublet distribution of density μ can be replaced by an equivalent surface vortex distribution (Hess (1972)) where the vortex sheet strength $\vec{\gamma}$ at each surface point satisfies the relation,

$$\vec{\gamma} = -\vec{n} \times \nabla\mu \tag{3.20}$$

A doublet panel with constant positive strength μ induces the same velocity field at every field point as a vortex loop with strength μ , provided that the edges of the doublet panel coincide with the vortex loop. In the current study, vortex loop panels were used rather than doublet panels.

3.2 *Formulation of the Problem*

Two types of vortex sheets were used for the present study; a bound vortex sheet which represents the wing surface, and a free vortex sheet which represents the wake flow. There is a pressure jump across the bound vortex sheet, while across the free vortex sheet there is no pressure difference. The trailing vortices, which model the wake, can be aligned either parallel to the free stream or parallel to the vehicle axis. Such an alignment would result in a linear problem. According to Bertin and Smith (1979) both orientations provide similar accuracy within the assumptions of linearized theory. In the present study the trailing vortices have been aligned parallel to the axis of symmetry of the wing.

The planform of the wing was divided into a finite number of panels. Each panel was made up of straight vortex filaments fixed at the edge of the panel, forming a closed vortex loop with constant circulation. Free vortex sheets were represented by free vortex filaments starting from the edge panels of the wing and extending to infinity. The panels on the edge of the wing formed closed vortex loops by including the vortex filaments at infinity which were starting vortices.

For the present study, the vortex lattice panels in the bound vortex sheet were shifted one quarter of the local panel chord. The vortex lattice panels have been located on the mean camber surface of the wing. The control point of each panel is centered spanwise on the three-quarter chordline of the panel.

Fig. 18 shows the panel arrangement for the rectangular wing with the gap. The solid lines represent the vortex loop panel and dashed lines represent the free vortex filaments. The edge of the wing is represented by a dotted line and the control points are denoted by (+) symbols. Considering the symmetry of the wing the vortex panels on one side of the axis of symmetry only need to be used in the computation. The gap at the root of the wing can be easily introduced in this formulation. It has been done by shifting the vortex loop panels by the size of the gap in the spanwise direction away from the axis of symmetry.

The Biot-Savart law (Eqn. 6.36 in Bertin and Smith (1979)) was used to calculate the induced velocity due to the segments of vortex filaments. Referring to Fig. 19, induced velocity at point P due to the vortex segment AB is,

$$\vec{V} = \frac{\Gamma}{4\pi h} \frac{\vec{r}_1 \times \vec{r}_2}{|\vec{r}_1 \times \vec{r}_2|} \left[\frac{\vec{r}_0 \cdot \vec{r}_1}{r_0 r_1} - \frac{\vec{r}_0 \cdot \vec{r}_2}{r_0 r_2}\right] \tag{3.21}$$

where $h = \frac{|\vec{r}_1 \times \vec{r}_2|}{r_0}$ and Γ = strength of the vortex filament.

Using the vortex loop panels, the governing equation (3.19) for a M paneled wing can be written as,

$$[A]\{G\} = \{R\} \tag{3.22}$$

A_{ij} is an element of the influence coefficient matrix and is the normal component of the induced velocity at the i-th control point by a vortex loop with unit strength at the j-th panel, G_j is the strength of the vortex loop at the j-th panel, and $R_i = -V_{\infty n i}$ is the normal component of the free stream velocity at the i-th control point. G_j was taken positive for the clockwise vortex loop which induced a velocity in the negative z direction in Fig. 18.

The boundary conditions for the current problem is that the flow must be tangential to the wing surface. (No normal velocity) As mentioned earlier, this is a linear problem. The solution vector $\{G\}$ was obtained using a readily available program from the International Mathematical and Statistical Libraries (ref.22), to solve linear equations.

3.4 Aerodynamic Load Calculation

The velocity jump across the vortex sheet is,

$$\Delta\vec{V} = \vec{\gamma} \times \vec{n} \tag{3.23}$$

The velocity discontinuity can not be obtained at the control point in a strict sense because the wing was modeled with vortex loop panels. The purpose of this computational program was not to find an exact solution, but an approximate solution was desired. Therefore the same order of approximation was required to obtain the velocity jump as the wing was modeled.

To obtain a velocity jump, the vortex loop panel was considered as a constant doublet strength panel since both panels produce the same induced velocity (Hess (1972)). Substituting the doublet-vortex relation (3.20) into the velocity jump-vortex strength relation (3.23), the velocity jump across a doublet panel is,

$$\begin{aligned} \Delta\vec{V} &= (- \vec{n} \times \nabla\mu) \times \vec{n} \\ &= - \nabla\mu \end{aligned} \tag{3.24}$$

Since the vortex loop panel is the same as the constant strength doublet panel, the velocity jump at the control point of the panel can be obtained by a mean slope of the doublet strength on a panel. Referring to Fig. 20 the mean slope of the doublet strength at the i-th panel is

$$\begin{aligned} - \mu_x &= \frac{\frac{1}{2}(G_{i+1} + G_i) - \frac{1}{2}(G_i + G_{i-1})}{l_x} \\ &= \frac{G_{i+1} - G_{i-1}}{2\, l_x} \end{aligned} \tag{3.25.a}$$

$$
\begin{aligned}
-\mu_y &= \frac{\frac{1}{2}(G_{i+n} + G_i) - \frac{1}{2}(G_i + G_{i-n})}{l_y} \\
&= \frac{G_{i+n} - G_{i-n}}{2\, l_y}
\end{aligned}
\qquad (3.25.b)
$$

Hence the velocity jump can be obtained directly from the strength of the vortex loop.

$$
\Delta \vec{V} = -\nabla\mu = \nabla G \qquad (3.26)
$$

A mean vortex strength can be obtained using equation (3.23) and equation (3.25)

$$
\begin{aligned}
\vec{\gamma} &= \vec{n} \times \Delta \vec{V} \\
&= \vec{n} \times \nabla G \\
&= \frac{G_{i+1} - G_{i-1}}{2\, l_x}\vec{j} - \frac{G_{i+n} - G_{i-n}}{2\, l_y}\vec{i} \\
&= \frac{[\, -G_{i+n}\, l_x \vec{i} + G_{i+1}\, l_y \vec{j} + G_{i-n}\, l_x \vec{i} - G_{i-1}\, l_y \vec{j}\,]}{(2\, l_x\, l_y)}
\end{aligned}
$$

choosing $\Gamma_1 = G_{i-n}$, $\Gamma_2 = G_{i+1}$, $\Gamma_3 = G_{i-n}$, $\Gamma_4 = G_{i-1}$, $\vec{l_1} = l_x \vec{i}$, $\vec{l_2} = l_y \vec{j}$, $\vec{l_3} = l_x \vec{i}$, $\vec{l_4} = l_y \vec{j}$, and

$A = l_x\, l_y$, then

$$
\vec{\gamma} = -\sum_{i=1}^{4} \frac{\Gamma_i \vec{l_i}}{2\, A} \qquad (3.27)
$$

Since there are no panels ahead of the leading edge for the rectangular wing, G_{i-n} is zero when i-th panel is on the leading edge. Hence the velocity jump and mean vortex strength become,

$$\Delta\vec{V} = \frac{G_{i+1} - G_{i-1}}{2\,l_x}\vec{i} - \frac{G_{i-n}}{2\,l_y}\vec{j} \tag{3.28}$$

$$\vec{\gamma} = -\sum_{i=2}^{4}\frac{\Gamma_i\vec{l_i}}{2\,A} \tag{3.29}$$

One can think that the doublet sheet is stretched to infinity from the trailing edge because the vortices are being shed from the trailing edge to infinity. If the i-th panel is on the trailing edge then G_{i-n} becomes G_i and the velocity jump and the mean vortex strength are,

$$\Delta\vec{V} = \frac{G_{i+1} - G_{i-1}}{2\,l_x}\vec{i} + \frac{G_{i+n} - G_{i}}{2\,l_y}\vec{j} \tag{3.30}$$

$$\vec{\gamma} = -\sum_{i=1}^{4}\frac{\Gamma_i\vec{l_i}}{2\,A} \tag{3.31}$$

where $\Gamma_3 = G_i$.

A similar relation can be applied to the side edge of the rectangular wing. The velocity jump can be calculated using equation (3.23).

After the velocity jump is obtained, the pressure can be found by using Bernoulli's equation. The total pressure was assumed to be constant in the flow field. Since only steady cases were considered,

$$P + \frac{1}{2}\rho V^2 = P_\infty + \frac{1}{2}\rho V_\infty^2 \tag{3.32}$$

The velocities on the upper surface and lower surface at the control point are,

$$\vec{V}_u = \vec{V}_\infty + \vec{V}_i + \frac{1}{2}\Delta\vec{V}$$

$$\vec{V}_l = \vec{V}_\infty + \vec{V}_i - \frac{1}{2}\Delta\vec{V} \tag{3.33}$$

The pressure coefficients for both surfaces become,

$$C_{pu} = 1 - (\frac{V_u}{V_\infty})^2$$

$$C_{pl} = 1 - (\frac{V_l}{V_\infty})^2 \tag{3.34}$$

The normal force coefficient and axial force coefficient are obtained by summing up the pressure differences multiplied by each panel area. The pitching moment was calculated about the leading edge of the wing.

$$C_N = \sum_{i=1}^{M}(C_{pl} - C_{pu})_i \frac{n_z A_i}{A}$$

$$C_A = \sum_{i=1}^{M} (C_{pl} - C_{pu})_i \frac{n_x A_i}{A}$$

$$C_M = \frac{\left[\sum_{i=1}^{M} (C_{pl} - C_{pu})_i \{ n_z(- x) + n_x z \} A_i \right]}{A\, c}$$

where A_i : area of the i th panel

A : total area of the wing projected on the x-y plane

c : mean aerodynamic chord

$x,\ z$: x and z coordinate of the i th control point

n_x, n_z : x, z component of the i th unit normal vector.

Then the lift coefficient and induced drag coefficient are,

$$C_L = C_N \cos\ \alpha - C_A \sin\ \alpha$$

$$C_{Di} = C_N \sin\ \alpha + C_A \cos\ \alpha \qquad (3.35)$$

A flow chart of the steps involved in this computation is shown in figure 21.

IV. Experimental Set-up and Operation

In addition to the computational evaluation, wind tunnel tests were set-up and run in order to evaluate the effect of the end plate gap. The computation simulates an inviscid flow over a rectangular wing. The behaviour of the Wortmann FX-63-137-ESM airfoil at low Reynolds numbers is unlike other airfoils like the Clark-Y airfoil. Some airfoil shapes do not exhibit classic low Reynolds number flow behaviour such as stall hysteresis in steady flow. The Clark-Y, which is the basis for the whole NACA 4 digit series of airfoils was shown by Marchman and Werme (1984) to exhibit only a weak stall hysteresis loop at low Reynolds numbers. The behaviour of the Wortmann airfoil is different due to certain low Reynolds number flow effects like the laminar separation bubble (Sumantran (1985), Abtahi (1985)). Also, the computation did not simulate the flow through the gap as there is no known method for doing the same. Hence, it was necessary to study the semi-span end plate gap effects in the wind tunnel.

In this chapter the wind tunnel, the model, the model support and the data acquisition technique used in the experiments are described. In addition, flow visualization of the flow through the gap was done. A description of the technique employed in the flow visualization is presented at the end of this chapter.

4.1 Wind-tunnel

The Virginia Tech Stability Wind-tunnel was used to conduct all experiments for this study. This is a single return subsonic wind-tunnel and was used with a $6' \times 6' \times 28'$ closed test section. The nozzle contraction ratio for this tunnel is 10 to 1. The tunnel is driven by a 14′ diameter propeller. The tunnel is capable of producing a steady flow for a velocity range from 20 ft/s to 240 ft/s in the test section. A schematic of this tunnel is presented in Fig.22. The large size of the tunnel enables testing even 3-dimensional models with negligible blockage effects.

The controls and instrumentation relating to data reduction and experiment control are located in an air-tight room surrounding the test section and accessible through an air lock. This permits easy test section accessibility for modifications and instrumentation without altering static pressure during testing. This control room also houses the instrumentation for wind-tunnel speed control.

4.2 Model and Model support

Testing was done with an aspect ratio two, semi-span model (effective full span aspect ratio of four). The model used was made of aluminum with a five inch chord section. The contour of the Wortmann FX-63-137-ESM airfoil section used for the model is presented in fig.2. The model used in this study was a section from the set of models that were constructed for studying the effects of aspect ratio and free stream disturbances by Sumantran (1985) and Abtahi(1985) at Virginia Tech. It was modified to mount vertically on the strut balance used in the experiments.

The entire strut was shrouded to prevent contamination of the model force data with the forces on the support structure. In addition, a flat plate (1′ × 1′) was mounted to the top of the strut shroud and the semi-span model was mounted to the balance through a hole in the plate. The flat plate with the hole was mounted with four corner screws, enabling easy adjustment to be parallel to the flow direction. The gap between the plate and the model was introduced by pulling out or pushing in the model rod in a sleeve through the hole in the plate. The model was held steady with three tightening screws. The gap was adjusted to the desired width with the help of feeler gauges. Sealing the gap usually causes contamination of the data, due to the contact between the plate (and thus the strut shroud) and the model through the seal. In the present study, a previously tested technique was employed to seal the gap. The seal used in the preliminary tests conducted at Virginia Tech was a thin strip of common, low density, foam rubber weather stripping cut to the airfoil shape. This seal was attached to the model at the root. To ensure a good seal and to reduce friction between the model and the plate through the foam stripping, the seal was soaked with light-weight machine oil. This seal proved effective and also non-contaminating as pertaining to the results.

The strut balance used in this experiment is a three component balance, measuring normal, axial and lateral forces. For the tests designed for the present research, axial and lateral force components were resolved to give lift and drag forces on the model. This balance was mounted to the tunnel's rotating strut balance platform. Thus, allowing the balance to be yawed i.e. model pitched, to any desired angle in the flowfield. The model was set up as shown in figure 23. Tests were run by setting the desired tunnel speed and rotating the model through a range of angles of attack from $-12°$ through $+30°$

4.3 Data Acquisition

All the force data presented here were obtained from the strain gauge strut and associated bridge amplifiers. The ST03M moment balance was removed from the 6-component SRI-ST03M strut to accommodate vertical mounting of the wing model. The strut has a maximum load rating of 200 lb normal load, and 100 lb each of axial and lateral loads. The SRI-ST03M unit was originally built by

NASA Langley and was later regauged before use at Virginia Tech Stability Tunnel. The output of the strain gauge is 0.001 volt per 25.0 lb. Noise generated in the amplifier can cause fluctuations of 1 micro-volt resulting in an accuracy of the force data of 0.025 lb. This accuracy was found acceptable for the Reynolds numbers of interest (100,000 and above).

In order to be able to obtain force data through the hysteresis loop, remote actuation of the model angle of attack was necessary. As mentioned earlier, the strut balance was mounted on a yaw turntable. The model angle of attack, i.e. the strut yaw angle was changed with the help of a switch which activates the motor that rotates the yaw turntable. The same switch also activates another motor which drives a mechanical meter to give a digital read-out of the set angle of attack. The switch and the related mechanism enable the angle of attack of the model to be increased or decreased remotely. The smallest change obtainable is 0.01 degrees. Thus, it was possible to rotate the model through stall and then reverse to capture the stall hysteresis behaviour.

A Hewlett-Packard 3052 Automatic Data Acquisition System in conjunction with a Hewlett-Packard 9836 Desktop Computer was used for the experiments. The HP9836 computer is particularly suited for automatic data acquisition with an internal memory of up to 1 megabyte and two flexible disk drives. All the software was written using HP Basic Version 2.0 which is a powerful language for interaction with peripheral devices. A HPIB 8 Bit parallel interface was used for communication between computer and externals.

All analog to digital voltage conversions were made using a Hewlett-Packard 3455A Digital Voltmeter (DVM) which has the capability of reading both AC and DC voltages at a resolution of 0.5 microvolts and a speed of up to 24 samples per second. Switching the channels that form the input to the DVM was achieved using a Hewlett-Packard 3495A Scanner. 5 out of a total of 40 channels were hardwired to fixed inputs such as tunnel temperature, static pressure, total pressure and the two force components. References (17) and (23) contain more detailed information with regard to interfacing techniques and the operation of the data acquisition system.

Test section static pressure, temperature and dynamic pressure were obtained through three of the five hardwired channels for data acquisition. A Validyne D899 electronic barometer was used to obtain the tunnel static pressure and a thermistor was used to read the tunnel temperature. The thermistor was mounted on a wooden base to achieve insulation from the control room. The tunnel dynamic pressure was obtained by using a pitot-static tube located near the model and connected to Datamatrix 1173 Electronic manometer which gave a reading in inches of water.

Figure 24 depicts the arrangement of the experimental set-up used for force data acquisition. The scanner is used to link the digital voltmeter to the 5 transducers. These are the 2 force transducers and the three for test section conditions, viz., temperature, static pressure and dynamic pressure. The computer can be triggered to read the register of the DVM.

The software developed to execute the complete experiment is presented in the form of a flow chart which is self-explanatory (Fig.25). Inputs to the program are the model and instrumentation data, and the number of samplings per data point. Usually 25 samples of each quantity were taken during data acquisition and averaged for each point. A tare reading was obtained prior to each run to account for any mounting variations as well as any residual voltages present in any of the channels. Two or more runs were usually conducted for each situation to ensure repeatability of the data. For each data point, the computer automatically reduced the data, created a printout and filed the data on a flexible disk.

4.3 Flow Visualization Technique

A visualization of the flow through the end plate gap was done to better understand the nature of the flow at the plate-model junction. For this purpose, tests were conducted using a technique developed by Peter Sutton of Cambridge University and introduced at Virginia Tech by William Devenport, a visiting research scientist.

The technique is termed as Surface-oil flow technique. The materials required for this technique are mainly, a special paint mixture for the flow visualization and a self-adhesive, black plastic film for the background. The special mixture was made using kerosene, titanium dioxide and oleic acid. Oleic acid is added so that the titanium dioxide moves in such a manner that fine streaks can be obtained. In order to contrast the white titanium dioxide a black plastic self-adhesive film was used as the background, thus enabling the streamlines on the surface to be seen clearly.

For the purpose of the present experiment, the black contact film was placed on the flat plate used earlier in the force tests. The black film was then coated thinly with the liquid suspension mixture using a paint brush. The wing was then put in place through the plate and the tunnel run steadily until the flow pattern was clearly visible on the film. The dried pattern was subsequently sprayed with artists fixative to preserve the flow pattern. This visualization technique was used with the gap open and also with the gap sealed.

V. Results and discussion

An attempt has been made to evaluate the effect of a gap on the lift of a rectangular wing using the vortex lattice method and then look at the experimental results in the light of those results.

5.1 Computational results

The computational results were obtained for a rectangular wing with semi-span AR of 2. The gap was introduced through specification of the co-ordinates of the wing. The gap parameter is defined as DEL = (gap width/semi-span length of the wing). Different values of DEL were used, to obtain results for different gap widths. Here, the results for DEL = 0.0, 0.02 and 0.04 are presented in figures 26 and 27. In order to observe the effect of the gap in the results, the width of the vortex panel, along the wing span, should be of the same order as the gap. Figure

26 shows the C_L vs. α curves for the three different gaps. It is clear that as the gap increases, there is a loss in lift. Figure 27 gives the Γ distribution along the wing span (the value 0.0 indicates the root) for the aforementioned gaps at a station 0.4166C from the leading edge for zero angle of attack. For DEL = 0.0, the distribution is that as obtained for a rectangular wing without a gap. The same figure compares the Gamma distribution on the wing with gaps, DEL=0.02 and 0.04, with that of no gap, DEL=0.0. It is clear from this figure that there is a loss in the lift loading near the gap and that the trailing vortices at the root affect the lift distribution along the span, as expected. This is due to the fact that the gap cannot sustain a pressure difference between the lower and upper surfaces. Therefore, Γ should go to zero at the end of the gap near the root, thus producing a gradient of Γ along the span of the wing , which results in trailing vortices. These trailing vortices in turn affect the lift distribution on the whole wing, as observed previously.

Alan Pope (1966) notes in his authoritative text on low speed wind tunnel testing, that it is hard to evaluate the effect of the slot between the model and the tunnel wall. He also mentions that theoretical considerations indicate that a slot will decrease the effective aspect ratio.Looking at figure 26 again; it is noticed from the C_L vs. α curves that there is a drop in $\frac{d(C_L)}{d\alpha}$ as the gap increases. Comparing, this with data for wings of different aspect ratios in figure 28, we can draw the conclusion that the gap effect is analogous to the effect of aspect ratio, in the manner that as the gap increases, the effect is that of a decrease in aspect ratio. This is due to the loss of lift near the root of the wing with the gap as compared to that of a wing without the gap. The lift obtained for the wing with a gap can be obtained for a wing of smaller aspect ratio without the gap i.e. there is an aspect ratio effect. This is further clear in the $C_L - C_{D_i}$ plot for the aforementioned cases, for DEL = 0.0, 0.02 and 0.04. This is presented here in figure 30. Comparing this with figure 29, $C_L - C_D$ curves for different aspect ratios, it is evident that the gap effect is analogous to the effect of aspect ratio.

Of course, when the wing aspect ratio is large then the gap effect may not be so severe, and so noticeable. Because the aspect ratio considered for testing at Notre-Dame and in this study at Virginia Tech is 2, it is necessary to consider the gap effect, as the changes in results due to the gap are considerable.

From the theoretical calculations we can conclude that a gap within the wing affects the lift of the wing. Now that it is expected that a gap makes a difference in a vorticity model analysis, we have to consider the experimental results carefully. It should be quite apparent that we can not see the effects of viscosity in the aforementioned modeling. In the actual experimental set up we encounter the plate boundary layer, the interaction between the plate and the wing at their junction, the separation bubble on the wing and any other phenomena introduced due to viscosity and the presence of the gap.

In the theoretical considerations, it was not possible to model all of the aforementioned phenomena. The theoretical model considers the trailing vortices produced due the gap and their influence on the lift distribution. It would take a great deal of effort and time to evaluate the combined effects of all the phenomena analytically.

5.2 *Experimental results*

Tests were run at Reynolds numbers of 100,000 , 150,000 and 200,000 at gap sizes of 0.1mm., 0.5mm., 1.0mm., 1.5mm. and 2.0mm. Also, the gap was sealed with foam rubber stripping soaked in oil and tests were run at Reynolds numbers of 100,000 , 130,000, 150,000 and 200,000. The results are presented here in figures 31 to 37.

All the figures compare $C_L - \alpha$ curves. Figure 31 compares the curves at a Reynolds number of 100,000. In this figure there is an apparent shift observed in zero-lift angle when the gap is sealed. The data fall essentially on the same curve for different gap sizes, different from the curve for the case of sealed gap.

Each of the figures 32 to 36 corresponding to gap sizes of 0.1mm., 0.5mm., 1.0mm., 1.5mm. and 2.0mm., respectively, compare the CL vs. alpha curves for different Reynolds numbers for each gap. In all of these figures there appears to be little or no shift in the zero-lift angle with a change in gap size from as large as 2.0mm. to as small as 0.1mm. For gap sizes of 1.0mm., 1.5mm. and 2.0mm. (figures 34, 35 & 36) the curves fall nearly on the same line with increasing Reynolds number. However, when the gap sizes are 0.1mm. and 0.5mm. (figures

32 & 33) the case of 100,000 Reynolds number shows a variation in $\frac{d(C_L)}{d\alpha}$, as compared to the curve for 150,000 Reynolds number. Also, there is no such variation observed when the Reynolds number was increased from 150,000 to 200,000. This was not observed when the gap size was increased.

Further, consider the case of the sealed gap, presented here in figure 37. These results do not change in any manner with increase in Reynolds number, except that $C_{L\,\max}$ occurs at a higher angle of attack. This is an effect expected with increase in Reynolds number.

Along with the lift coefficient data, drag coefficient data was obtained for the aforementioned cases. Despite the low values of the force components contributing to the drag, it was possible to record sensible data in the Reynolds numbers range dealt with in the experiments. Figures 38 to 44 compare the different curves obtained for the same range of gap widths and Reynolds numbers as for lift coefficient curves. Though there is a lot of scatter in the data for the Reynolds number of 100,000, the general trend of the curves can be seen at this Re. The drag coefficient is generally higher when the gap was sealed than when the gap was open.

Figure 38 compares the different curves obtained at a Reynolds number of 100,000 for different gap widths including the sealed case. The striking difference in the value of minimum drag is apparent from the figure. The $C_{D_{\min}}$ has the highest value for the case of the sealed gap and decreases to a minimum for the case of the 2.0 mm. gap. This decrease in $C_{D_{\min}}$ is probably due to the leakage from the windward side to the leeward side through the gap. This leakage would decrease the pressure difference between the upper and lower surfaces, thus causing , not only a decrease in lift, but also a decrease in drag.

Figures 39 to 43 show the $C_D - \alpha$ curves for the cases of 0.1 mm., 0.5 mm., 1.0 mm., 1.5 mm. and 2.0 mm. gaps respectively. In all of these cases the classic Reynolds number behaviour of, first a decrease in $C_{D\min}$ and then an increase after reaching a minimum is observed. For the 0.1 mm. gap, the $C_{D_{\min}}$ decreases with Reynolds number until Re=200,000. It is the same behaviour for the case of 0.5 mm. gap too. For the cases Of 1.0 mm., 1.5 mm. and 2.0 mm. gaps, the $C_{D_{\min}}$ remains essentially the same. However, at higher angles of attack; for 1.0 mm. gap Re=200,000 has higher values of C_D and for 1.5 mm. gap Re=150,000 has higher values of C_D. In both cases Re=100,000 has the smallest C_D values. In the case of the 2.0 mm. gap the data fall essentially on the same curve, similar to the observations of Mueller et al (1986), figure 13.

Finally, figure 44 presents the $C_D - \alpha$ curves for the case of the sealed gap at different Reynolds numbers. This figure represents the normal behaviour of C_D with variation of Reynolds number. This figure further reinforces the observation that different results are obtained with tests conducted on a semi-span configuration with an end plate gap as compared to other test methods.

5.3 Flow Visualization

Tests were run using the previously explained technique for flow visualization. Two cases were run at a Reynolds number of about 100,000 ; one with the gap open and one with the gap sealed. The gap size for the open gap case was about 1.0 mm. The angle of attack for both the cases was held near zero. The results from these tests are presented here. Figure 45 was obtained for the case of the open gap and figure 45 for the case of the sealed gap. The outline of the Wortmann FX-63-137 airfoil has been sketched into figure 46. In the same figure, the black circle inside the airfoil profile indicates the hole for the wing mounting rod.

There is a striking difference in the flow patterns shown in figures 45 and 46. Figure 45 shows a significant flow through the open gap over the rear half-chord of the wing. This flow apparently causes early separation on the upper surface of the airfoil. This is the probable cause for the reduction in lift noted in the force tests conducted with the gap open. The flow visualization does not show the extent to which separation occurs along the span. Yet, the aforementioned figures clearly indicate that problems will be encountered while attempting to test a semi-span model with an end-plate/model gap which is not sealed effectively.

The figures obtained through the flow visualization as described in this study should be considered with caution. The flow pattern presented in these figures is due to the flow behaviour on the plate due to the presence of the wing. The flow is both due to the thin boundary layer on the flat plate and the flow around the wing. Hence, it is not proper to assume that the flow pattern duplicates the flow due to the free-stream alone. However, the flow patterns appear to show considerable detail regarding the flow about the wing, including thin separation bubbles on both the upper and lower surfaces and trailing edge separation subsequent to a noticable thickening of the upper surface boundary layer.

VI. Conclusions and Recommendations

6.1 Conclusions

The discrepancies in the aerodynamic performance data obtained at different test facilities for the Wortmann FX-63-137 airfoil and wing have been investigated. The size of the hysteresis loop is influenced by the tunnel environment. However, the Reynolds number effect observed in the data generated at Notre Dame and not observed elsewhere remained unexplained. These facilities use different mounting methods for testing wings. The single strut mounting method has already been investigated at Virginia Tech and was found to interfere negligibly with the flow on the wing model. Theoretical and experimental evaluations of the half wing model mounted with a gap at the end plate were performed.

A vortex panel method was used for the theoretical analysis. The size of the panel in the direction of the span, was of the order of the gap size to sense the influence of the gap on the results. The results were found to confirm Pope's (1966) statements. The end plate gap was found to have the effect of reducing the aspect ratio of the wing in the C_L - α and C_L - C_{D_i} curves obtained. The vorticity distribution along the span also shows this effect. Thus a loss of lift was observed in the theoretical results. These results indicate the existence of a problem due to the gap. However, these results compare poorly with experimental results. This is to be expected in view of the non-duplication of the flow through the end plate gap and the boundary layer on the end plate in the theoretical model.

Experiments were conducted at different Reynolds numbers for different gap widths at the end plate with a half wind model of an effective aspect ratio of 4. The results obtained indicate the following features:

1. There is a definite loss in the lift in the presence of a gap, due to enhanced separation on the leeward side, thus producing a shift in the zero lift angle of attack.

2. The C_L - α curves show a shift to the left, as observed in the Notre Dame data.

3. Even for a gap as small as 0.1 mm., the effect of the gap on the results is evident.

4. The C_D values obtained were observed to be generally less than those obtained without the gap.

5. Inspite of these effects some general trends in the behaviour of the wing were observed. For example an increase in the stalling angle of attack as Re increases along with the classical effect of Reynolds number on $C_{D_{\min}}$ were observed in the results.

6. Flow visualization at the plate-wing intersection shows how the flow through the gap changes the separation pattern on the airfoil near the plate.

6.2 Recommendations

In view of the results of this research some recommendations can be made regarding aerodynamic testing at low Reynolds numbers,

1. Results obtained for small aspect ratio half wing models with end plate gaps should be corrected for gap effects or better, an effective seal should be used.

2. To enable the exploitation of the advantages of half model testing in simplicity of rigging and easy experiment control while keeping the errors to a minimum, further investigation for gap effects on different aspect ratio models is necessary.

References

1. Abtahi, A.A. and Marchman, J.F., "Aerodynamics of an aspect ratio 8 wing at low Reynolds numbers ", AIAA, Vol. 22, No.7, pp. 628-634, July 1985.

2. Abtahi, A.A., "Aspect ratio effects on wings at low Reynolds numbers ", Ph.D. Dissertation, Virginia Tech, May 1985.

3. Bastedo, W.G. and Mueller, T.J., "Performance of finite wings at low Reynolds numbers " UNDAS-CP-77B123, Univ. of Notre Dame, pp. 195-205, June 1985.

4. Bertin, J.J. and Smith, M.L., "Aerodynamics for engineers ", Prentice-Hall Inc., New Jersey, pp. 191, 1979.

5. Dyer, D.J. and Stollery, J.L., "Preliminary measurements of the flight performance of an RPV compared with wind-tunnel and CFD estimates ", Proceedings of the international conference on Aerodynamics at low Reynolds numbers, R.Ae.S., Paper no.29, October 1986.

6. Galbraith, R.A.McD., "The aerodynamic characteristics of a GU25-5(11)8 aerofoil for low Reynolds numbers ", Experiments in fluids, Vol 3, pp. 253-256, 1985.

7. Hess, J.L., "Calculation of potential flow about arbitrary three-dimensional lifting bodies ", MDC-J5679-01, McDonnel Douglas, October 1972.

8. Lissaman, P.B.S., "Low Reynolds number airfoils ", Annual Review of Fluid Mechanics, Vol.15, pp. 223-239, 1983.

9. Marchman, J.F., Abtahi, A.A., Sumantran, V. and Sun, Z., "Effects of aspect ratio on stall hysteresis for the Wortmann airfoil", AIAA Paper No.85-1770, AIAA, August 1985.

10. Marchman, J.F., Sumantran, V. and Schaefer, C.G., "Acoustic and turbulence influences on stall hysteresis ", AIAA Paper No.86-0179, AIAA, January 1986.

11. Marchman, J.F. and Sumantran V., "A comparison of finite wing low Reynolds number airfoil data", Dept. of Aerospace and Ocean engineering, Virginia Tech, Blacksburg, VA, July 1985.

12. Marchman, J.F. and Werme, T.D., "Clark-Y airfoil performance at low Reynolds numbers", AIAA Paper No.84-0052, AIAA, January 1984.

13. Miley, S.J., "A catalog of low Reynolds number airfoil data for wind turbine applications", Dept. of Aerospace engineering, Texas A&M University, February 1982.

14. Mueller, T.J., "Low reynolds vehicles", AGARDograph No.288, AGARD, February 1985.

15. Mueller, T.J., Batill, S.M., Brendel, M., Perry, M.L., Bloch, D.R., Hubner, A.F., Bastedo, W.G., O'Meara, M.M. and Schmidt, G.S., "Low Reynolds number wind tunnel measurements: the importance of being earnest", Proceedings of the international conference on Aerodynamics at low Reynolds numbers, R.Ae.S., Paper no.14, October 1986.

16. Pope, A. and Harper, J.J., "Low-speed wind tunnel testing", John Wiley and Sons, New York, pp.153 , 1966.

17. Programming techniques for the HP9836 Desktop computer, H-P Desktop Computer Division, Fort Collins, Colorado, 1976.

18. Render, P.M., "Airfoil measurements at low Reynolds numbers", COA Report No.8508, Cranfield, England, May 1985.

19. Rogers, E.W.E., "A background to the problems of wind-tunnel interference", AGARD Report 292, March 1959.

20. Sumantran, V., "The effect of free stream disturbances and control surface deflections on the performance of the Wortmann airfoil at low Reynolds numbers", Ph.D. Dissertation, Virginia Tech, October 1985.

21. Sun, Z., Sumantran, V. and Marchman, J.F., "An examination of flow and environmental effects on chordwise pressure distribution data on a finite

Wortmann wing at low Reynolds numbers", VPI-Aero-149, Dept. of Aerospace and Ocean engineering, Virginia Tech, Blacksburg, VA, July 1985.

22. The IMSL Library, International Mathematical and Statistical Libraries, Inc., Houston, Texas, 1977.

23. 3052 Automatic data acquisition system guide, H-P Desktop Computer Division, Fort Collins, Colorado, 1976.

24. van der Bliek, J.A., "Notes on half-model testing in wind-tunnels", AGARD Report 298, March 1959.

25. Williams, B.R., "The prediction of separated flow using a viscous-inviscid interaction method", ICAS paper 84-2.3.3, 1984 (see also RAE Tech. Memo 2010, 1984).

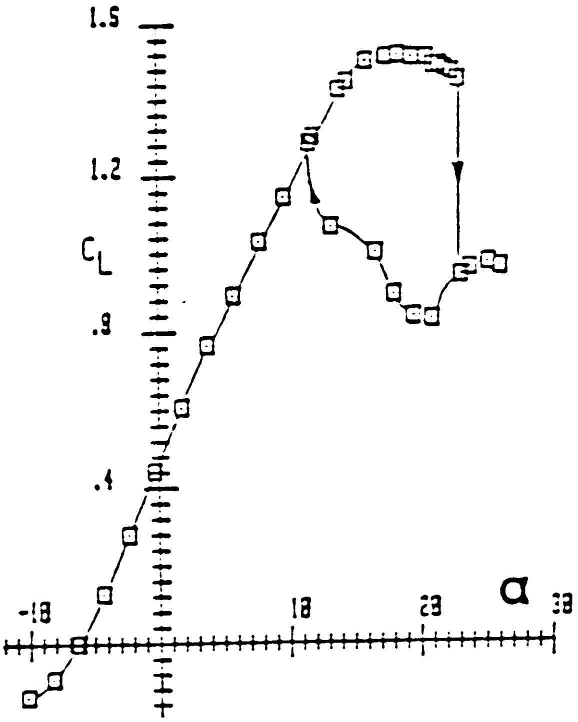

Figure 1. Stall hysteresis loop phenomena for an AR = 8, Wortmann airfoil at Re = 200,000 (Marchman and Abtahi 1985)

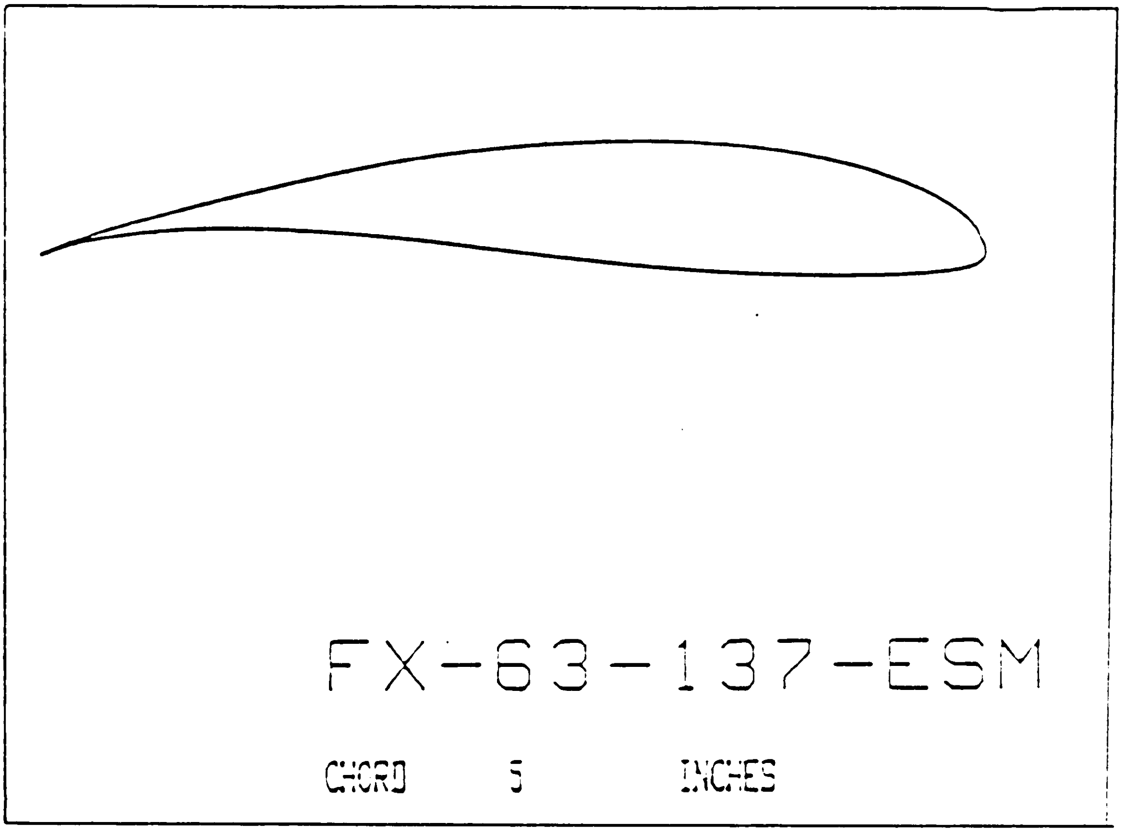

Figure 2. Wortmann FX-63-137-ESM airfoil contour.

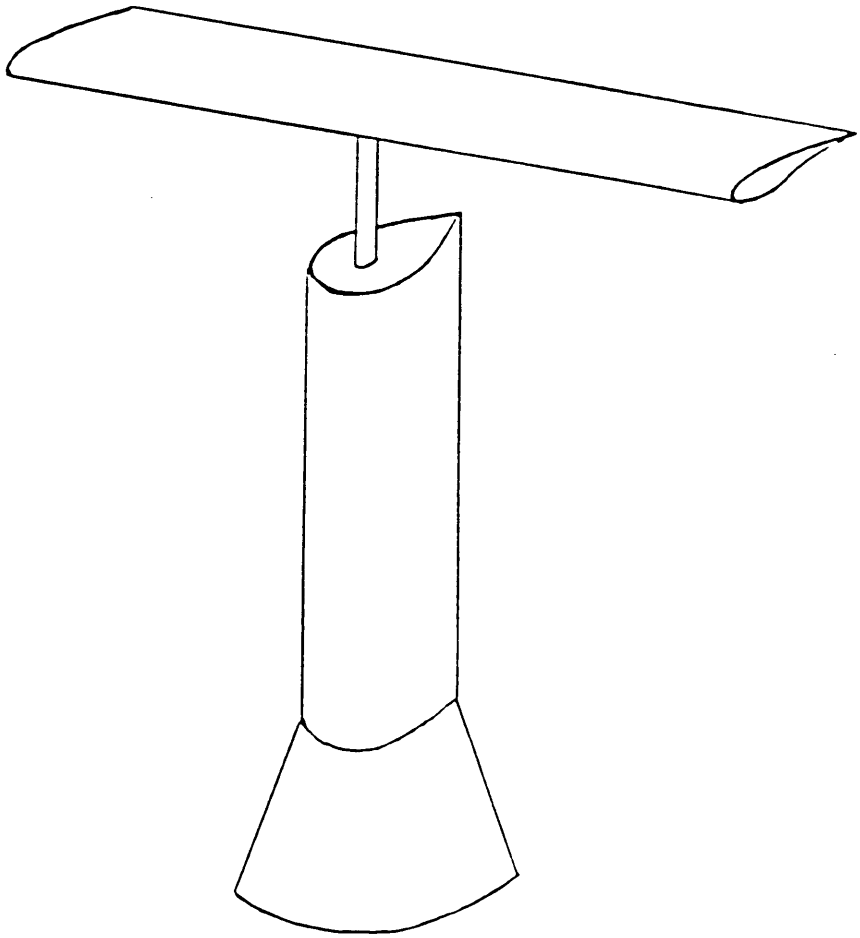

Figure 3. Single strut arrangement for a 3-dimensional wing model.

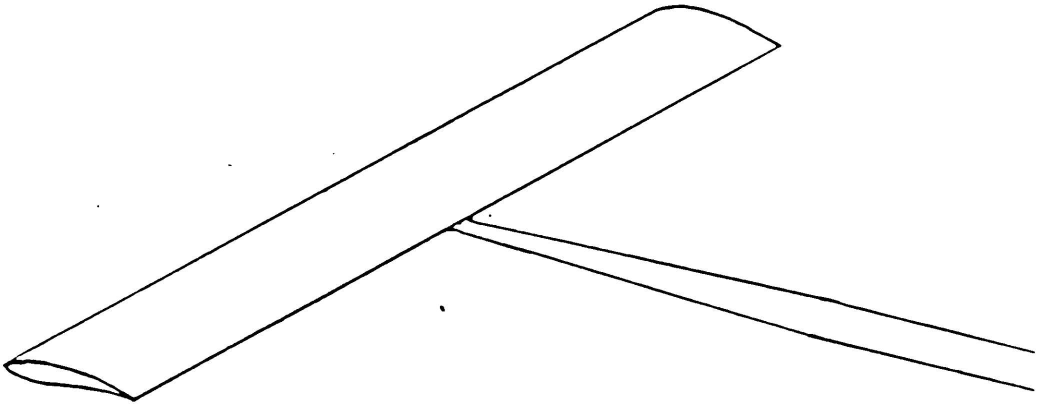

Figure 4. 3-dimensional wing with sting for sting mounting.

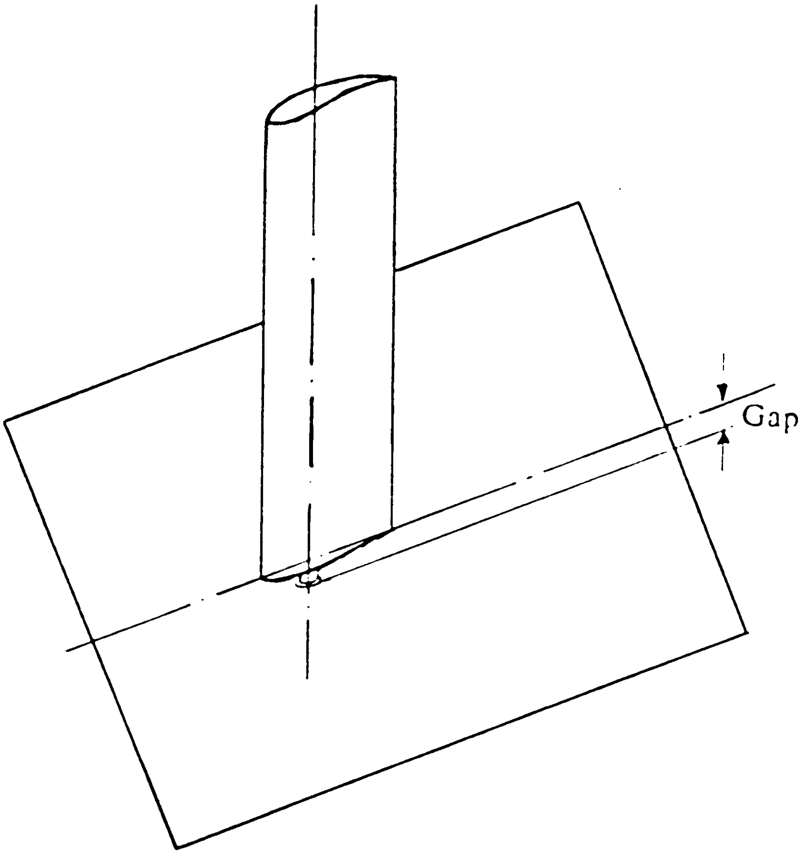

Figure 5. Short strut arrangement for a half wing model.

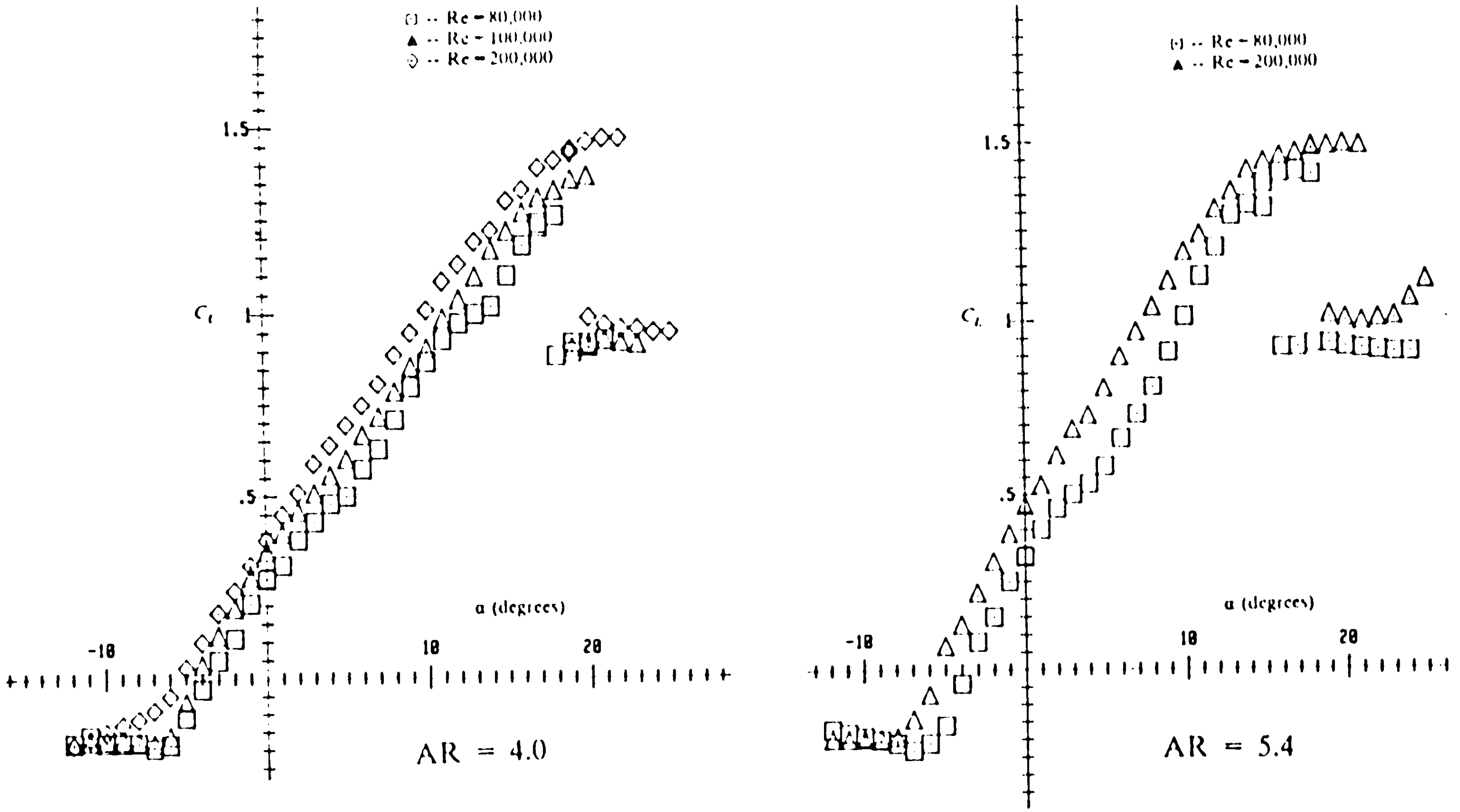

Figure 6. Notre Dame results for the Wortmann airfoil at different Reynolds numbers.

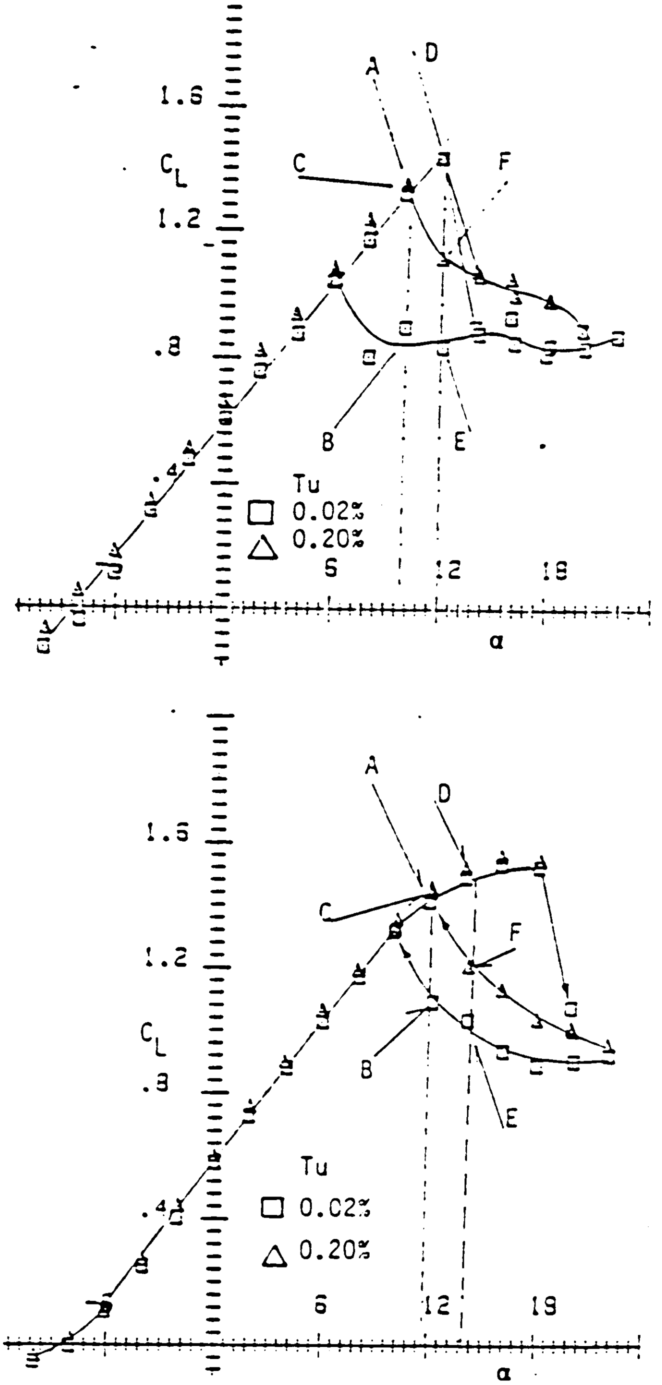

Figure 7. Influence of increased turbulence for AR = 8 wing at Re = 200,000 and 100,000 (Marchman, Sumantran and Schaefer, 1985).

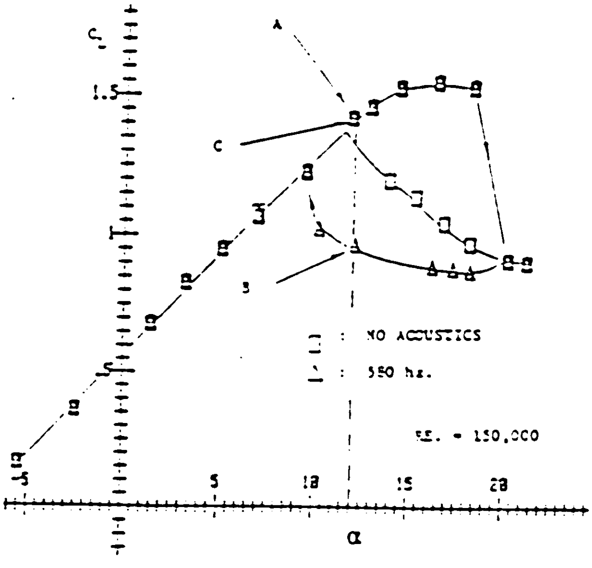

Figure 8. Influence of acoustic disturbance for 580 Hz., 0.5 W signal at Re = 150,000 (Marchman, Sumantran and Schaefer, 1985).

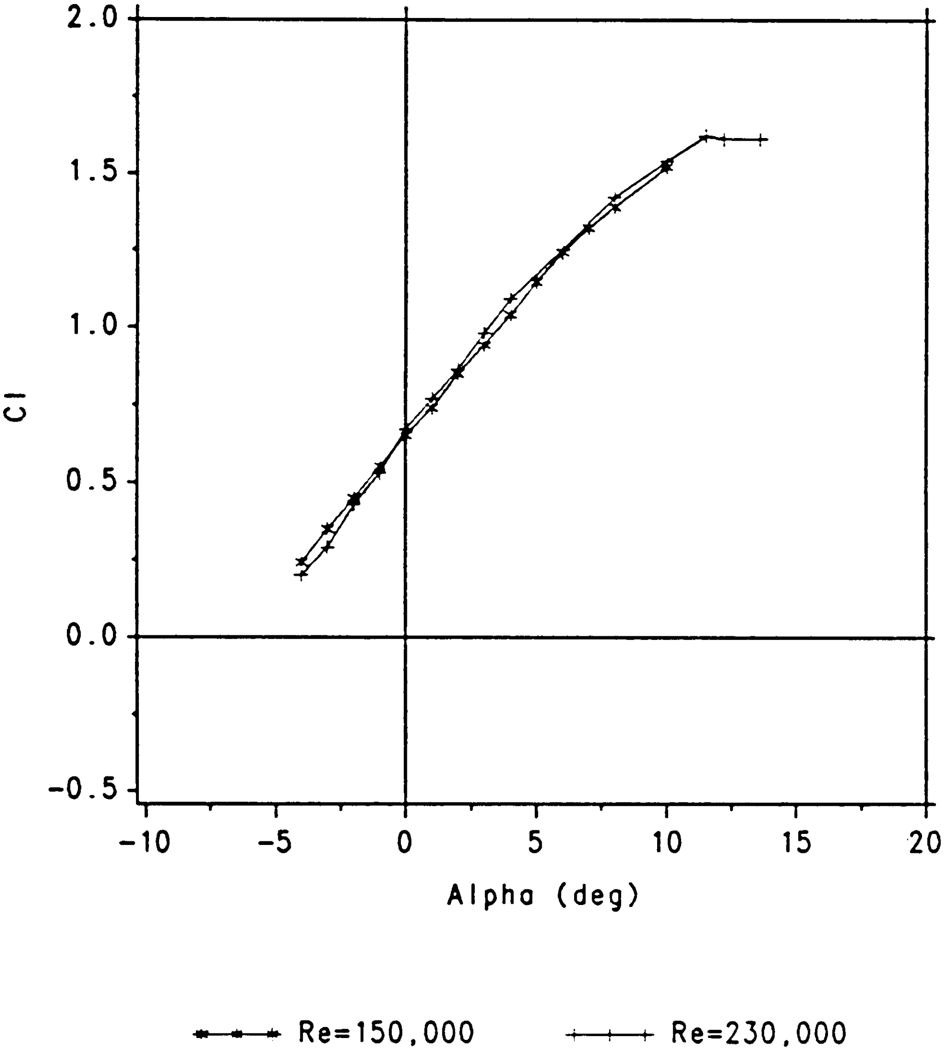

Figure 9. Stuttgart results for the Wortmann airfoil at different Reynolds numbers.

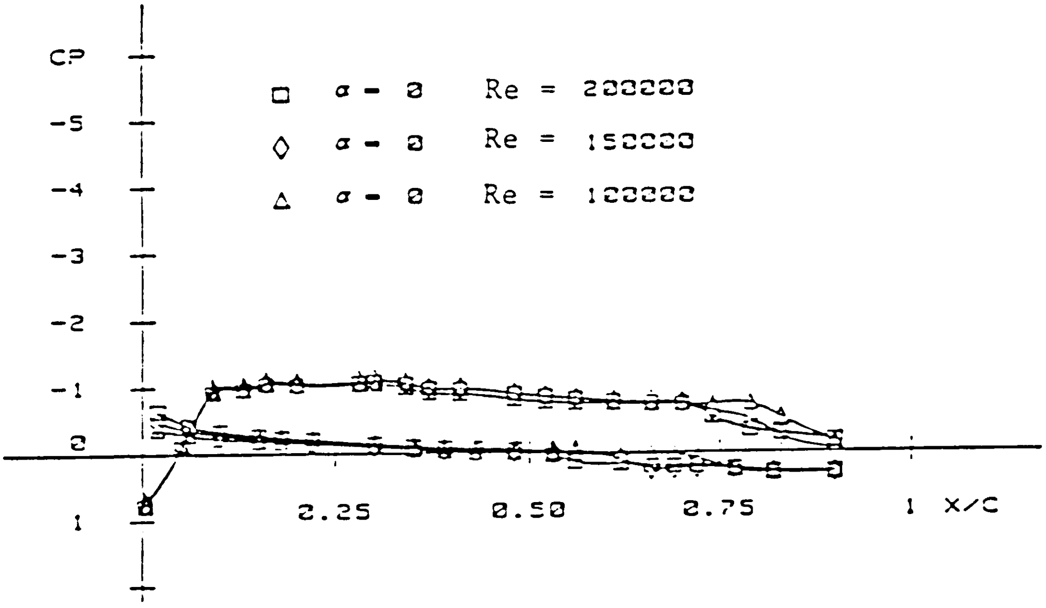

Figure 10. Variation of pressure distribution with Reynolds number (Marchman and Sumantran ,1985).

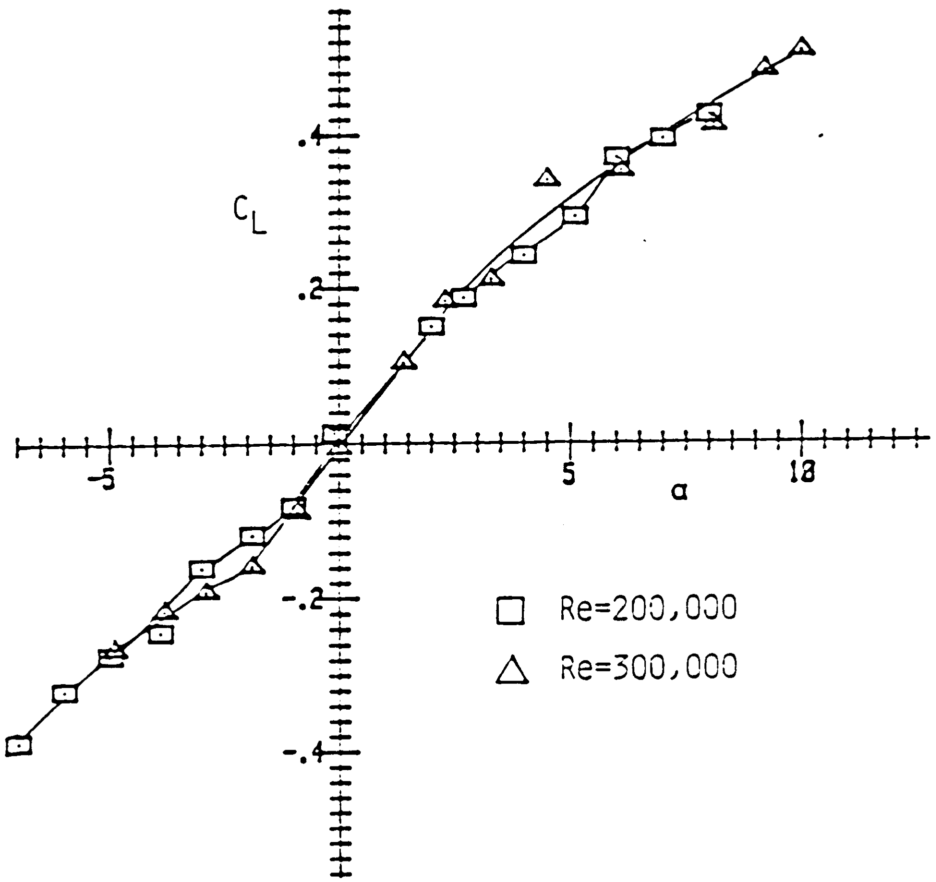

Figure 11. Test results for strut mounted flat plate, AR=6, at different Reynolds numbers (Marchman and Sumantran ,1985).

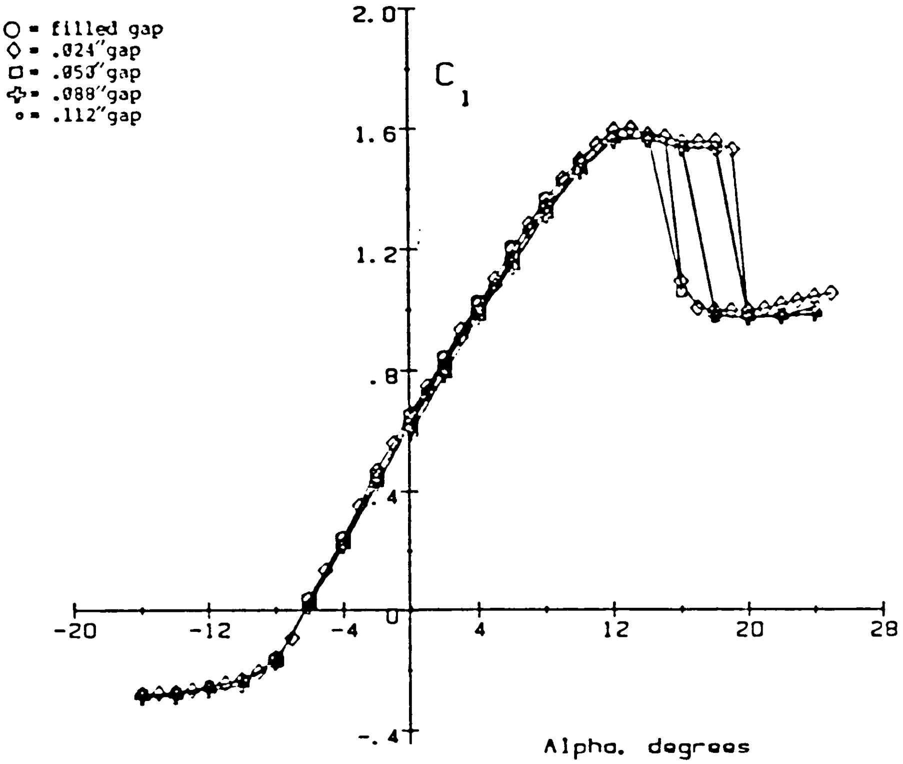

Figure 12. The effects of end gap spacing on the lift characteristics of the Wortmann airfoil at Re = 150,000 (Mueller et al., 1986).

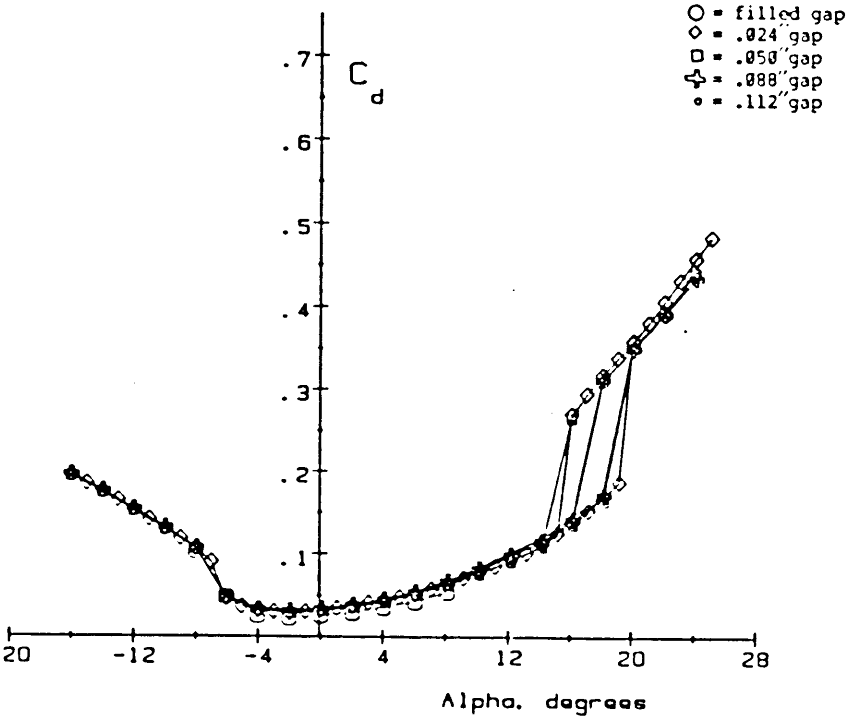

Figure 13. The effects of end gap spacing on the drag characteristics of the Wortmann airfoil at Re = 150,000 (Mueller et al., 1986).

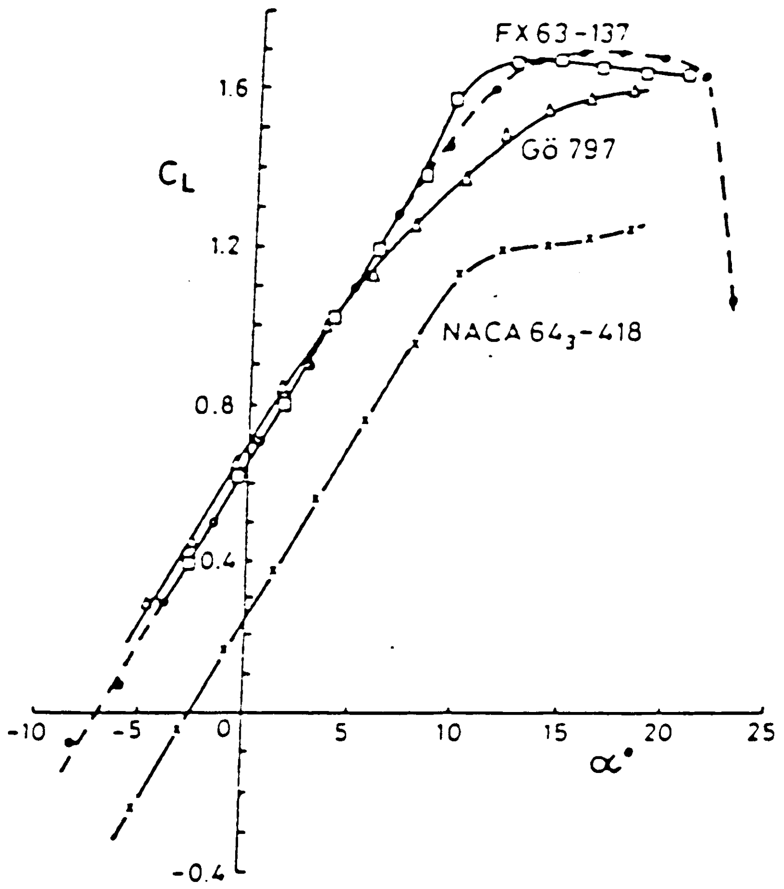

Figure 14. $C_L - \alpha$ curve for three airfoils including the Wortmann airfoil at Re = 300,000 (Dyer and Stollery, 1986).

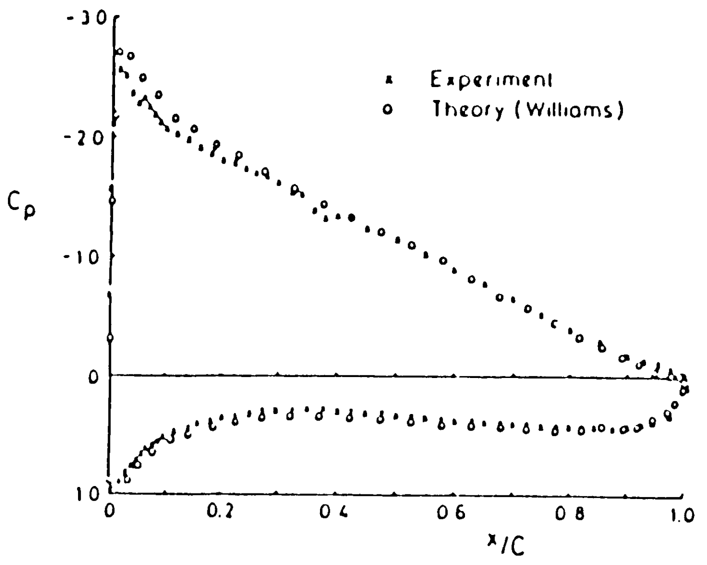

Figure 15a. Pressure distribution for Wortmann FX63-137 (CIT geometry), 8° incidence, Re = 0.7 x 10⁶.

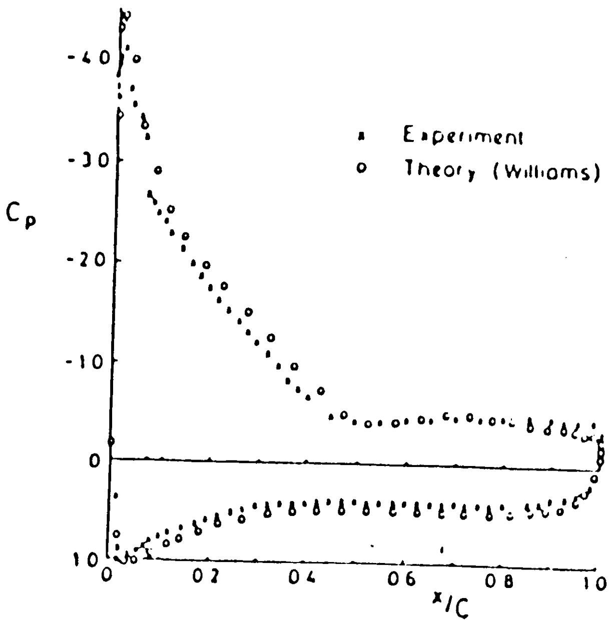

Figure 15b. Pressure distribution for Wortmann FX63-137 (CIT geometry), 16° incidence, Re = 0.7 x 10⁶.

Figure 15. Comparison of theoretical and experimental pressure distribution for Wortmann airfoil at incidences of 8° and 16° (Dyer and Stollery, 1986).

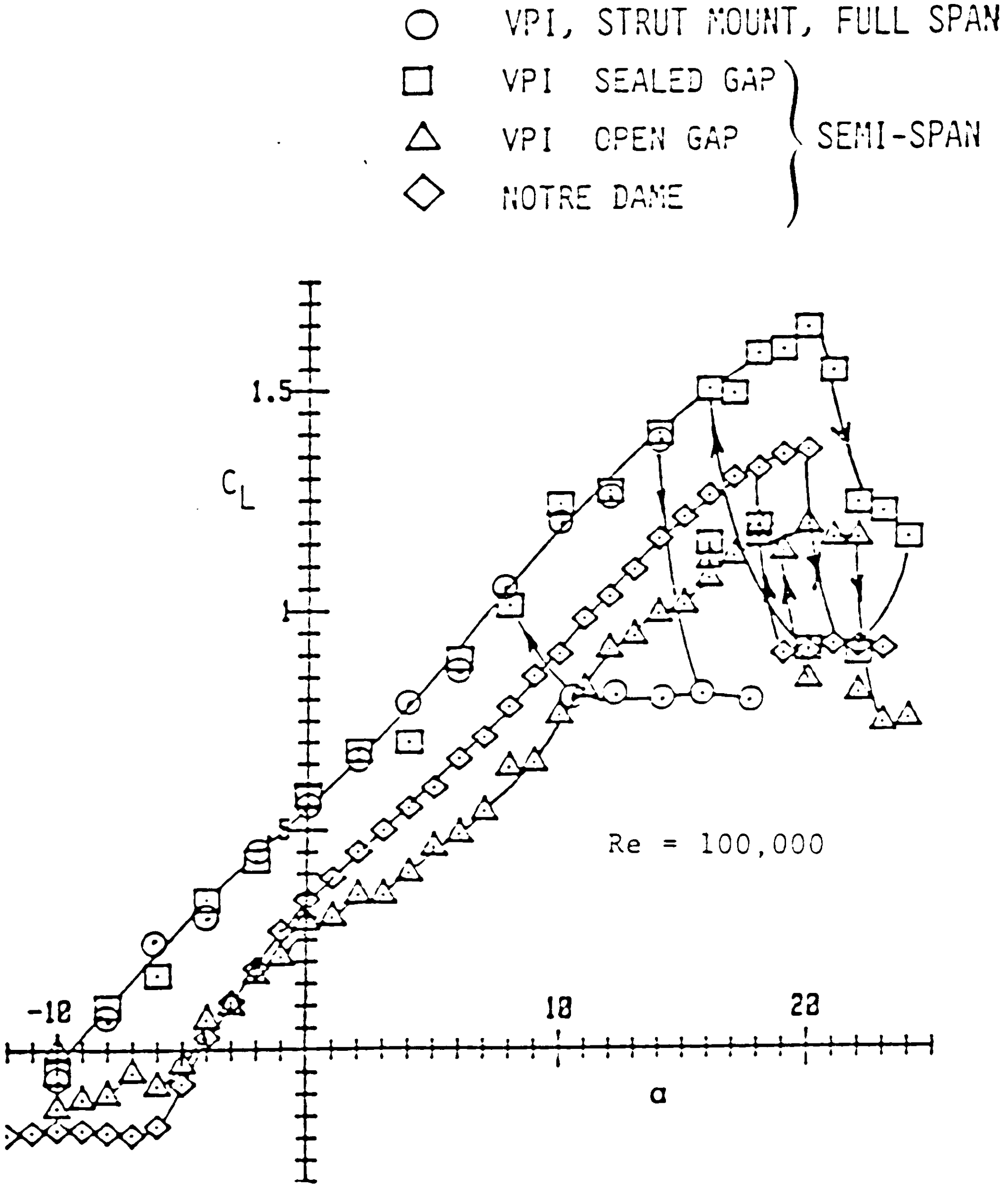

Figure 16. Preliminary results of the effect of sealing the end plate gap on semi-spanwing, AR = 4 (Marchman and Sumantran, 1985).

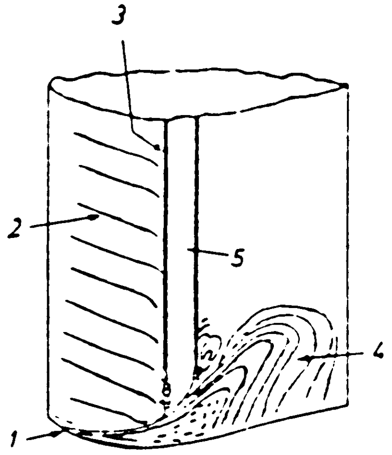

1. Laminar separation.
2. Typical streaks.
3. Oil fall due to gravity.
4. Vortex.
5. 2-D separation bubble.

Figure 17. Typical flow pattern at wall junction, Re=610,000 (Galbraith, 1985).

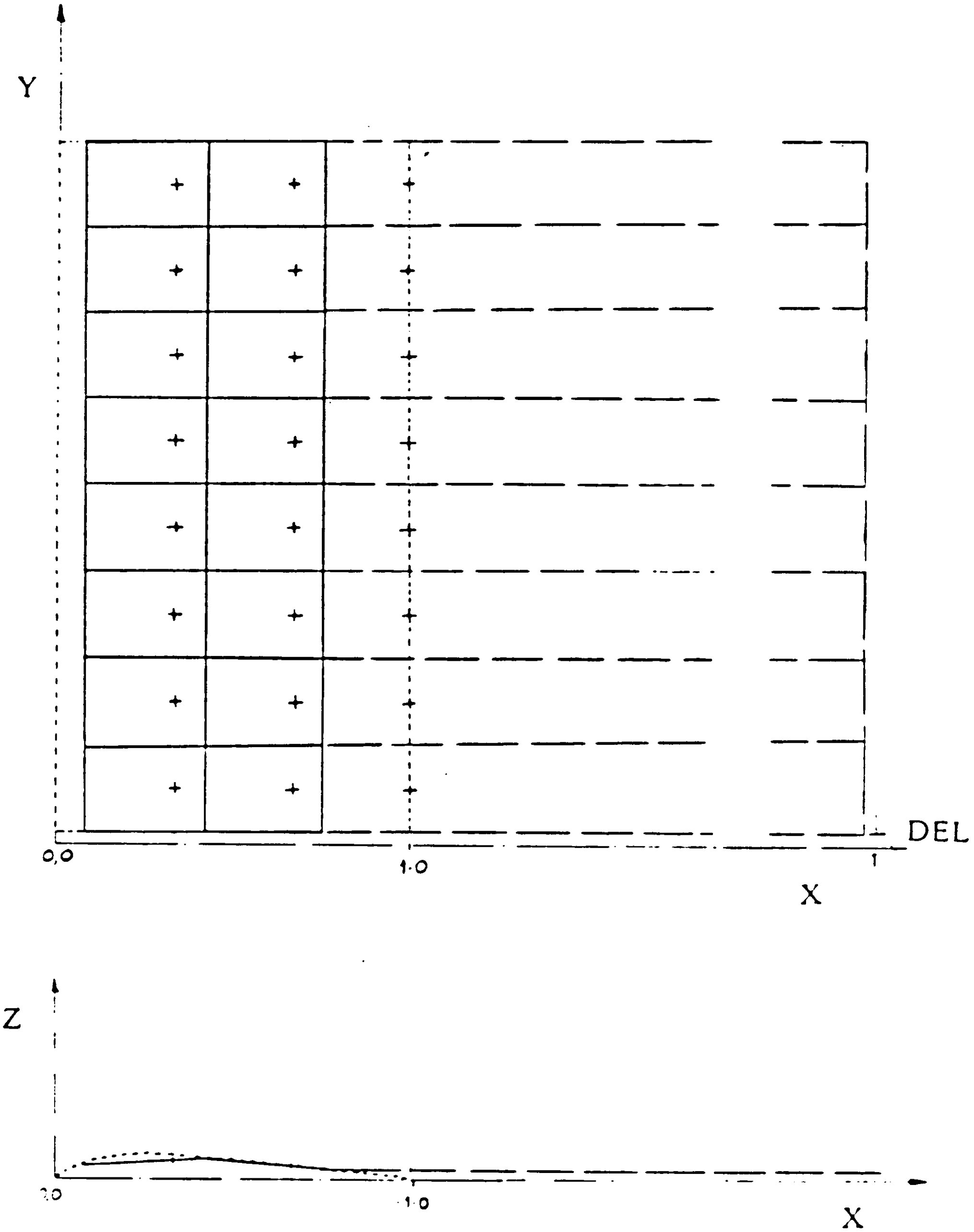

Figure 18. Vortex panel arrangement for a rectangular wing with a mid-span gap.

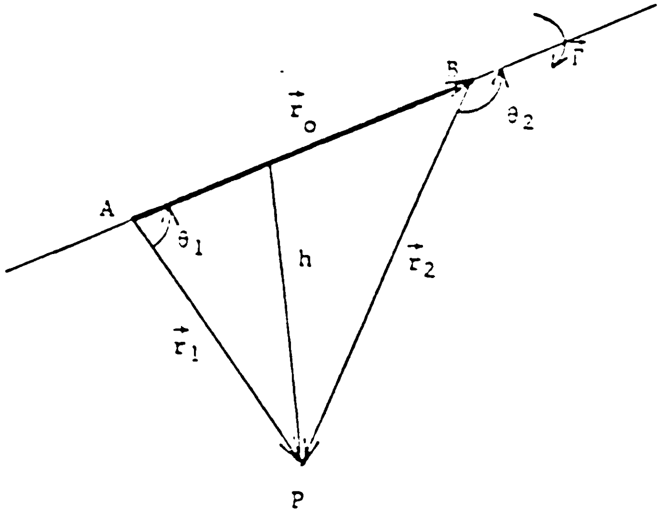

$$\vec{r}_0 = \overrightarrow{AB}$$
$$\vec{r}_1 = \overrightarrow{AP}$$
$$\vec{r}_2 = \overrightarrow{BP}$$
$$h = \frac{|\vec{r}_1 \times \vec{r}_2|}{r_o}$$

Figure 19. Notation for Biot-Savart law.

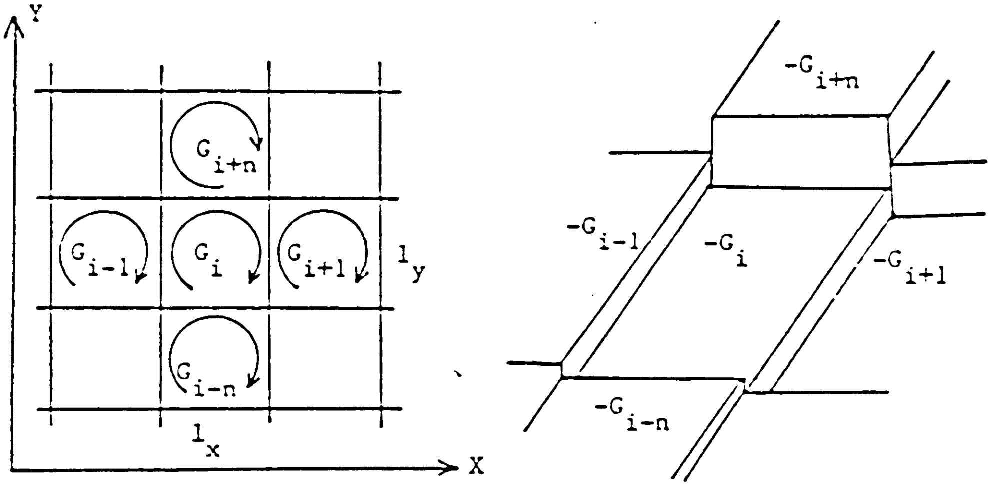

VORTEX LOOP PANEL DOUBLET PANEL

RECTANGULAR PANEL

Figure 20. Notation for velocity jump formula.

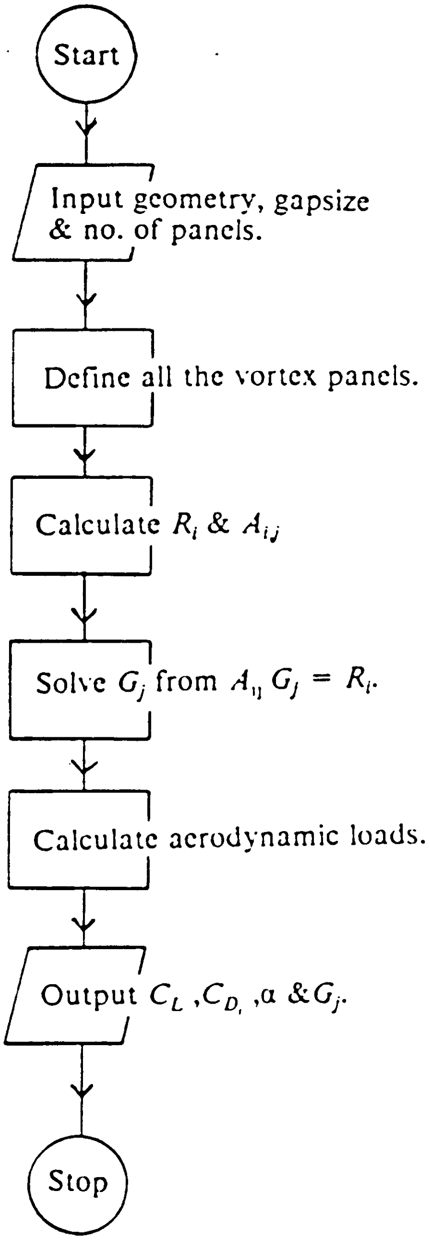

Figure 21. Flow chart of the program used in computation.

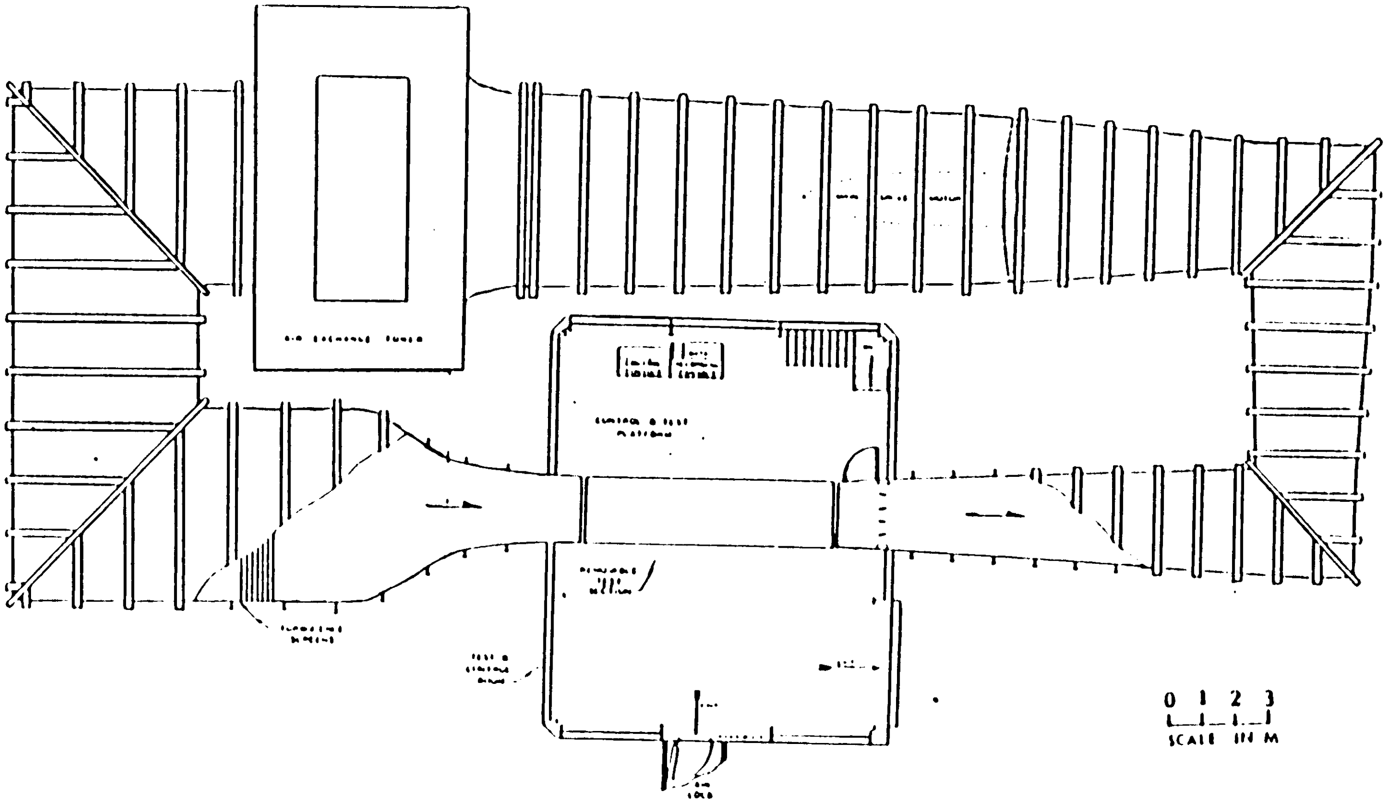

Figure 22. Schematic of the VPI&SU Stability Wind Tunnel.

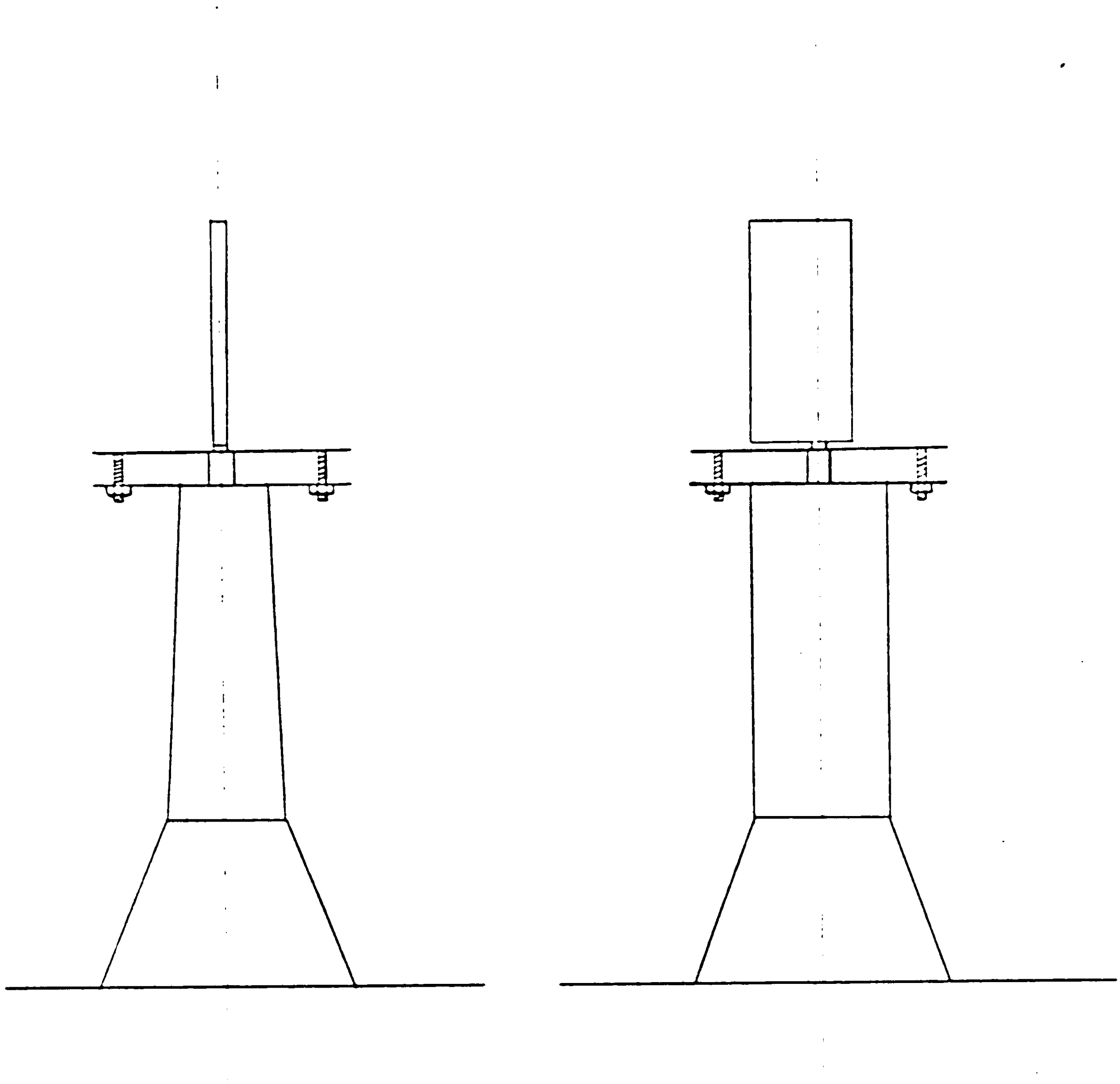

FRONT VIEW

SIDE VIEW

Figure 23. Set up of the model for experiments.

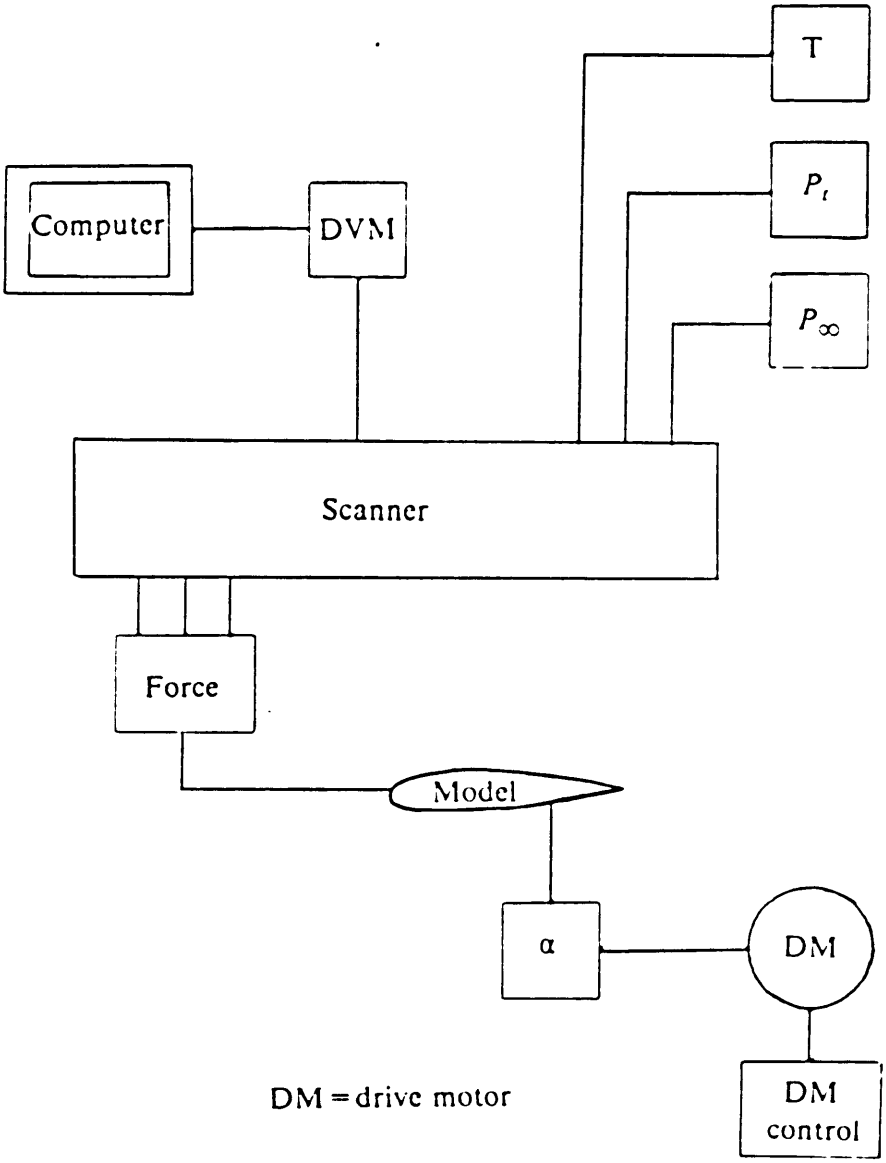

Figure 24. Set up of data acquisition system.

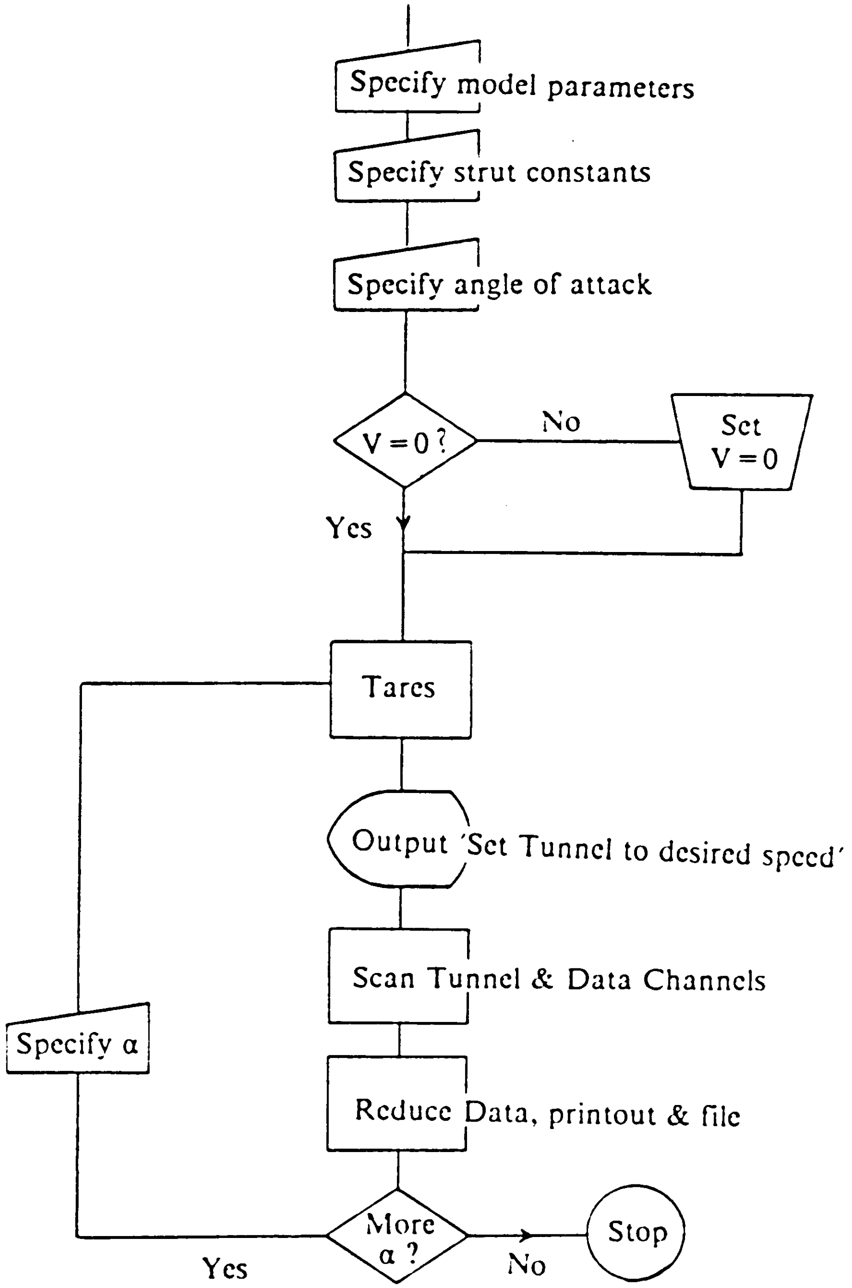

Figure 25. Flow chart for data acquisition program.

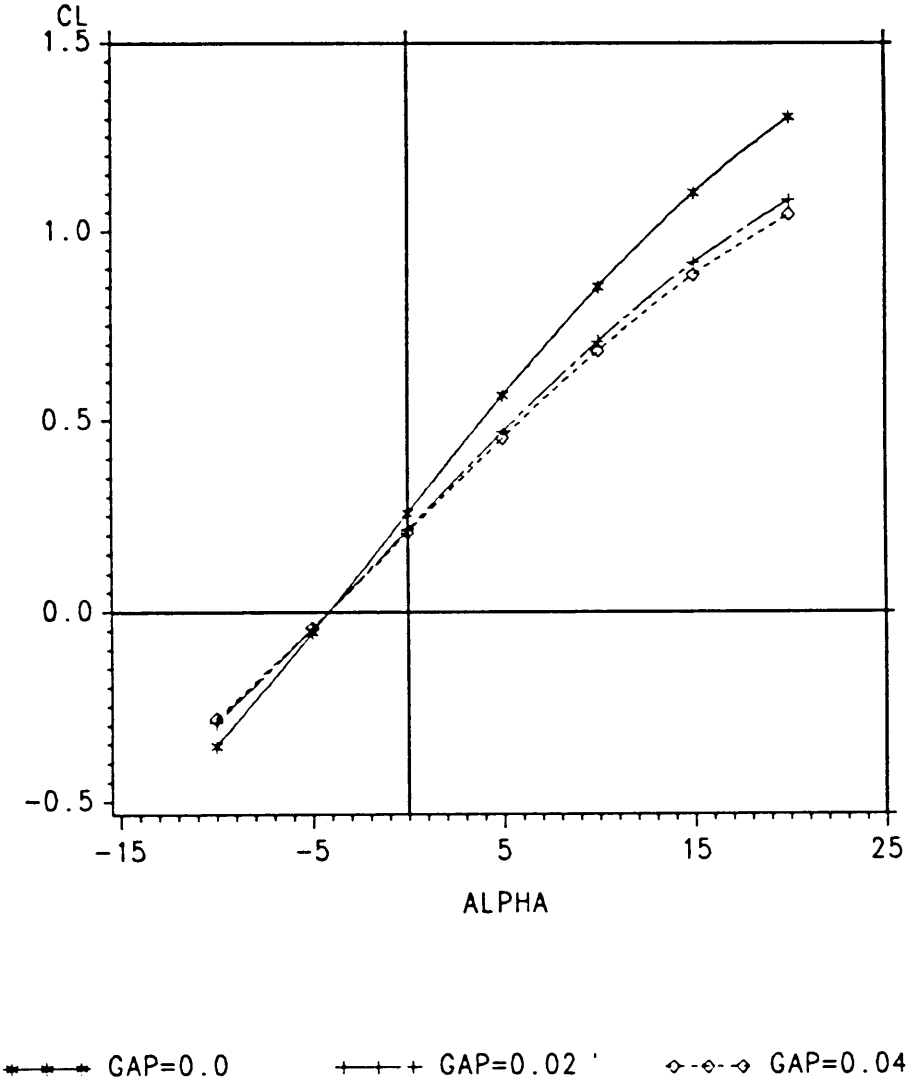

Figure 26. Computational results of the effect of gap on the lift characteristics.

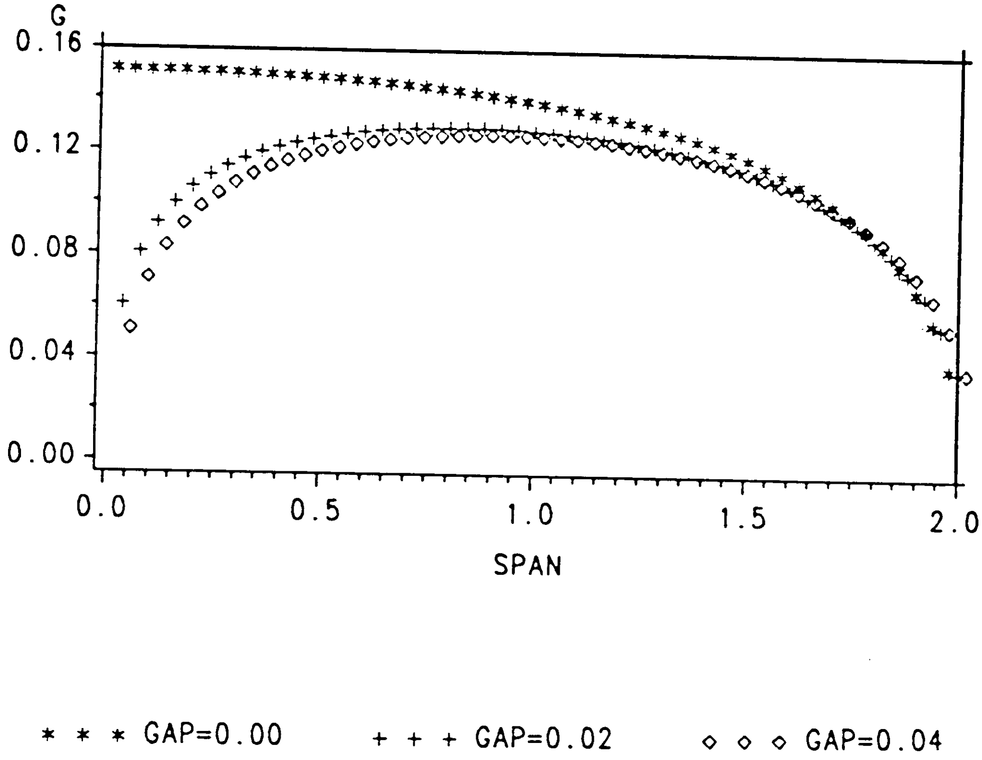

Figure 27. Computational results of the effect of gap on the vorticity distribution along the span of the wing.

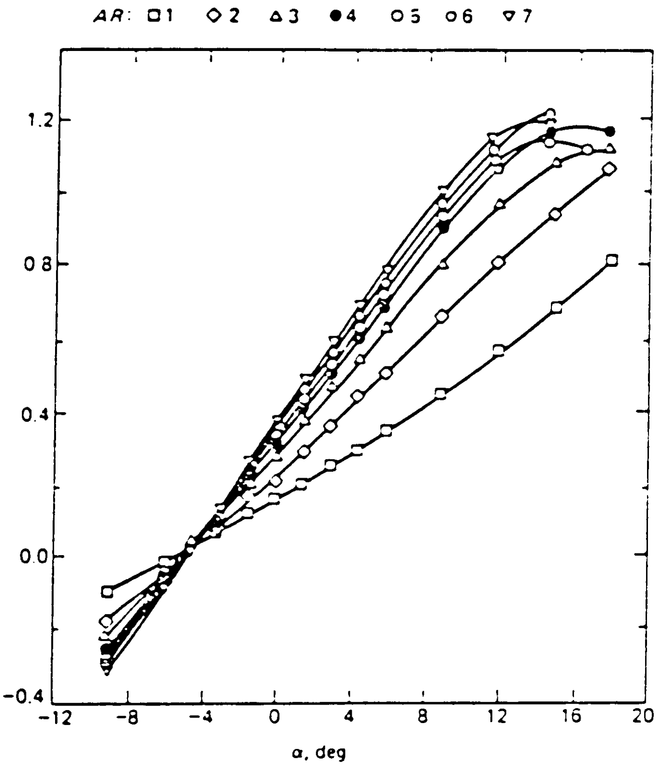

Figure 28. $C_L - \alpha$ curves for wings of different aspect ratios (Bertin and Smith, 1979).

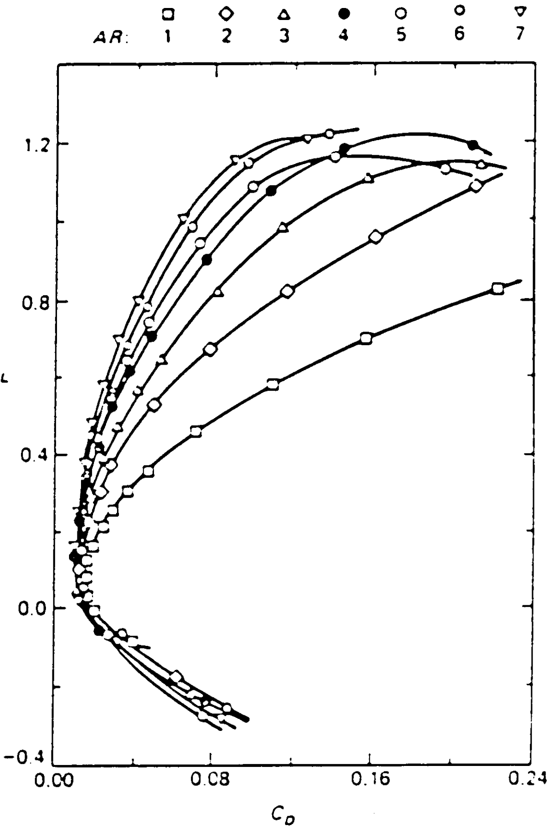

Figure 29. $C_L - C_D$ curves for wings of different aspect ratios (Bertin and Smith, 1979).

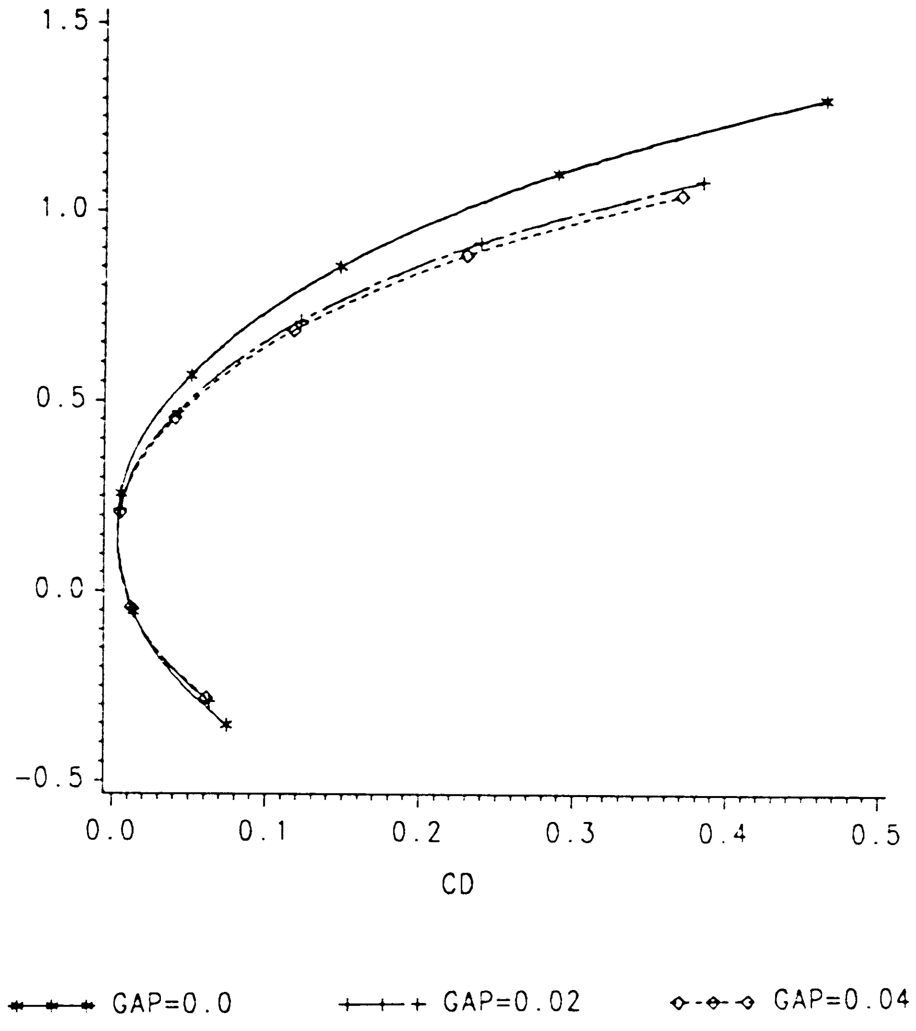

Figure 30. $C_L - C_{D_i}$ curves obtained by computation for different gap sizes.

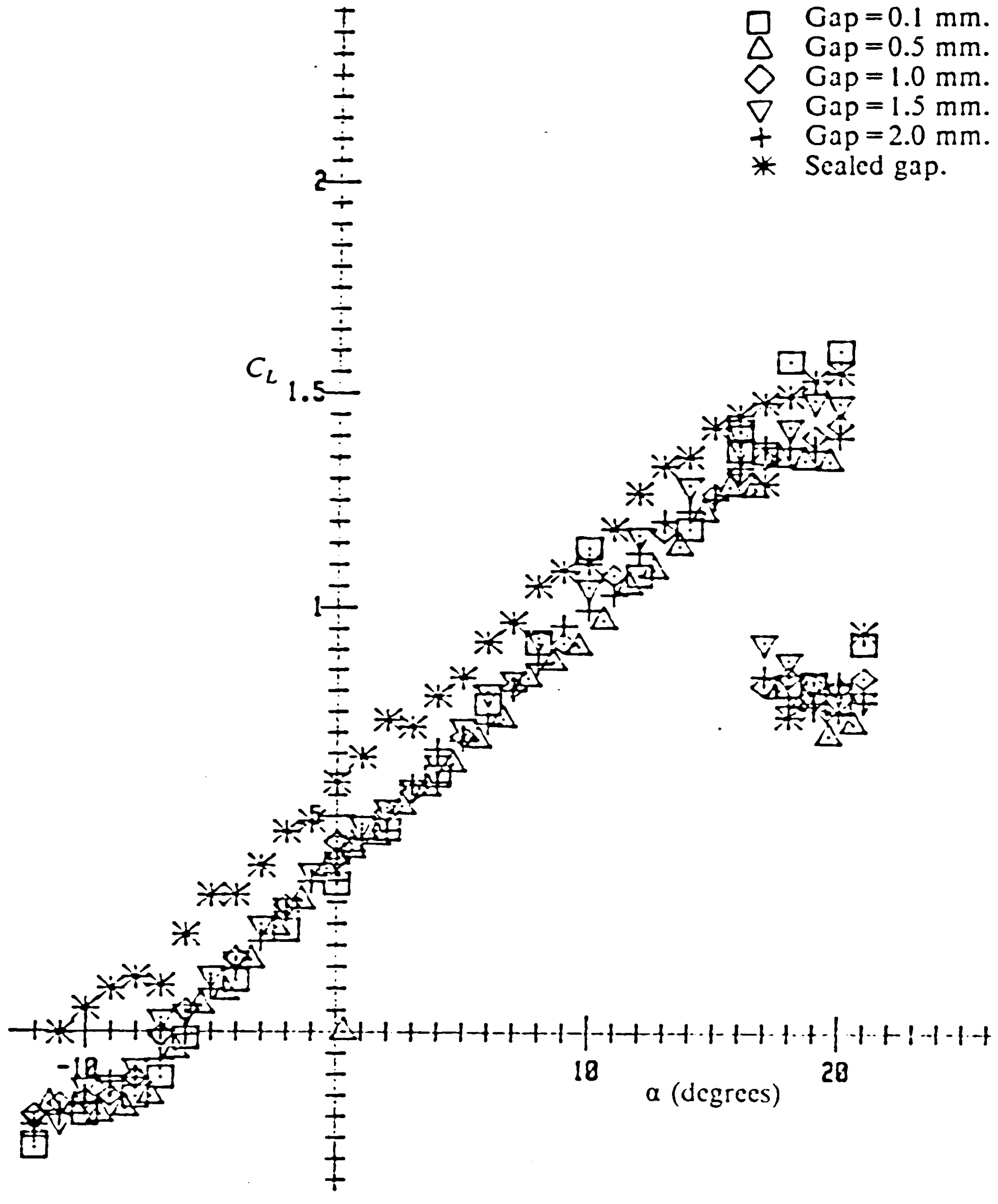

Figure 31. C_L − α curves at Re = 100,000 for different gap sizes including sealed gap.

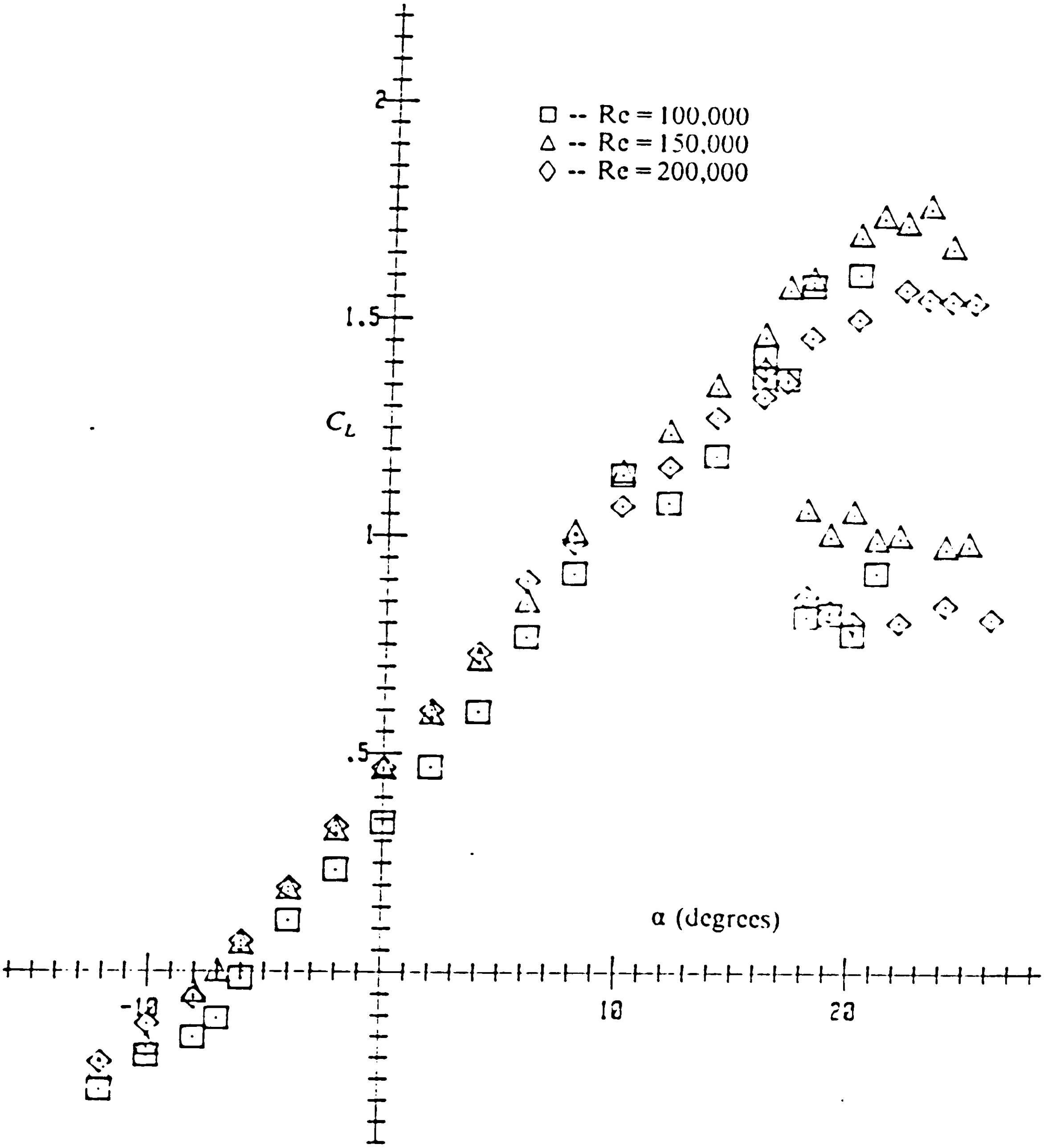

Figure 32. C_L − α curves for 0.1 mm. gap at different Reynolds numbers.

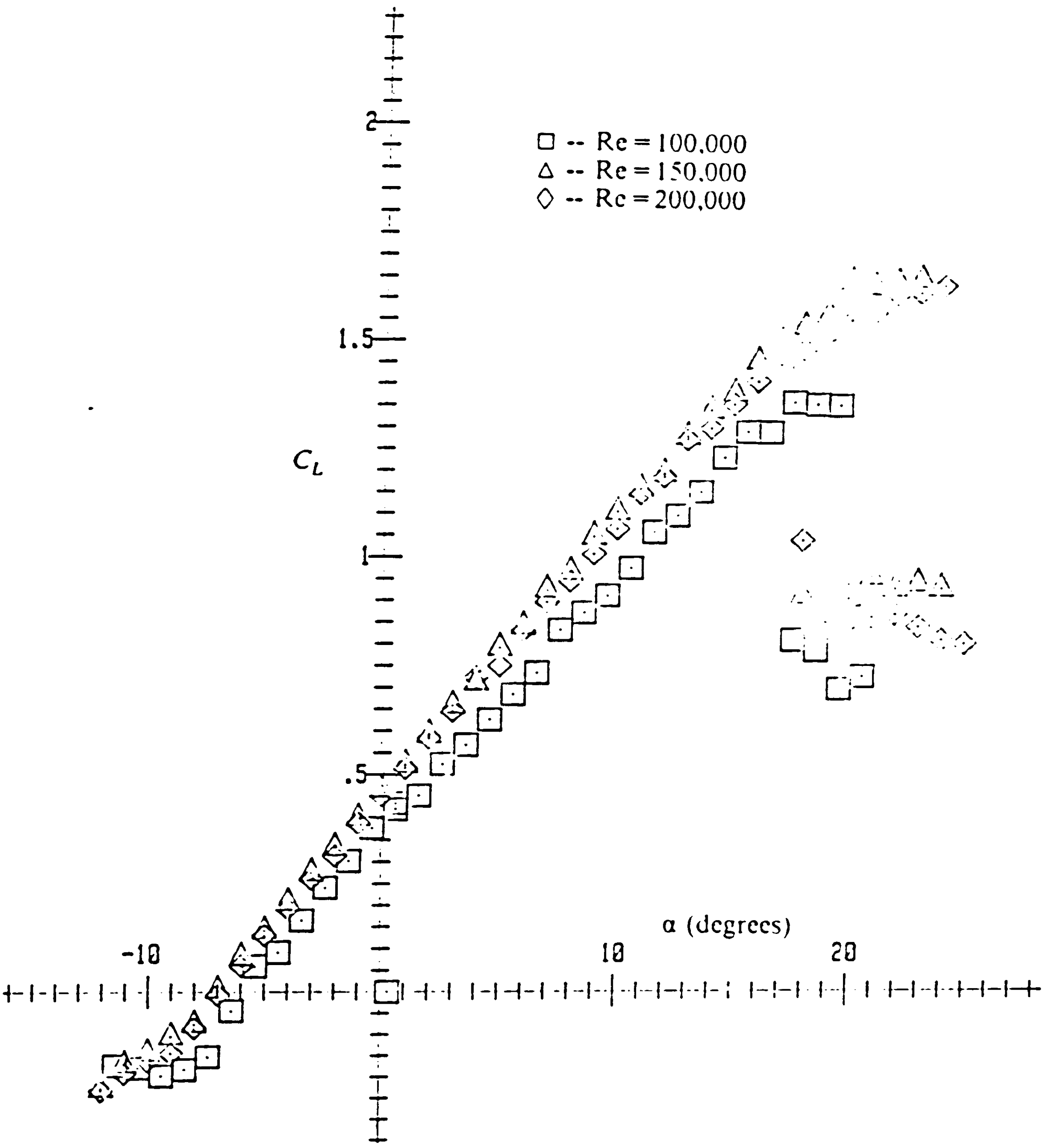

Figure 33. C_L – α curves for 0.5 mm. gap at different Reynolds numbers.

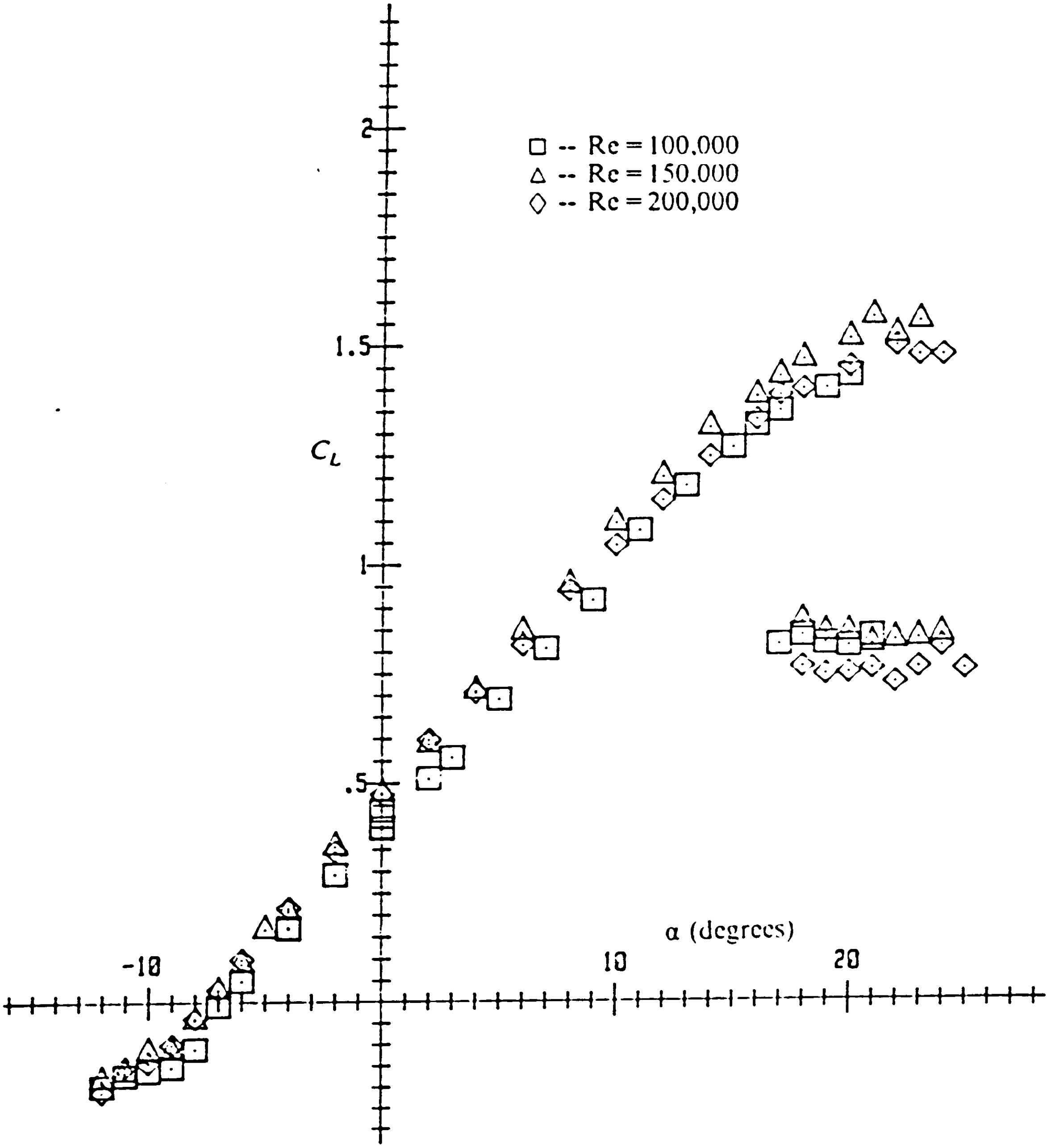

Figure 34. C_L − α curves for 1.0 mm. gap at different Reynolds numbers.

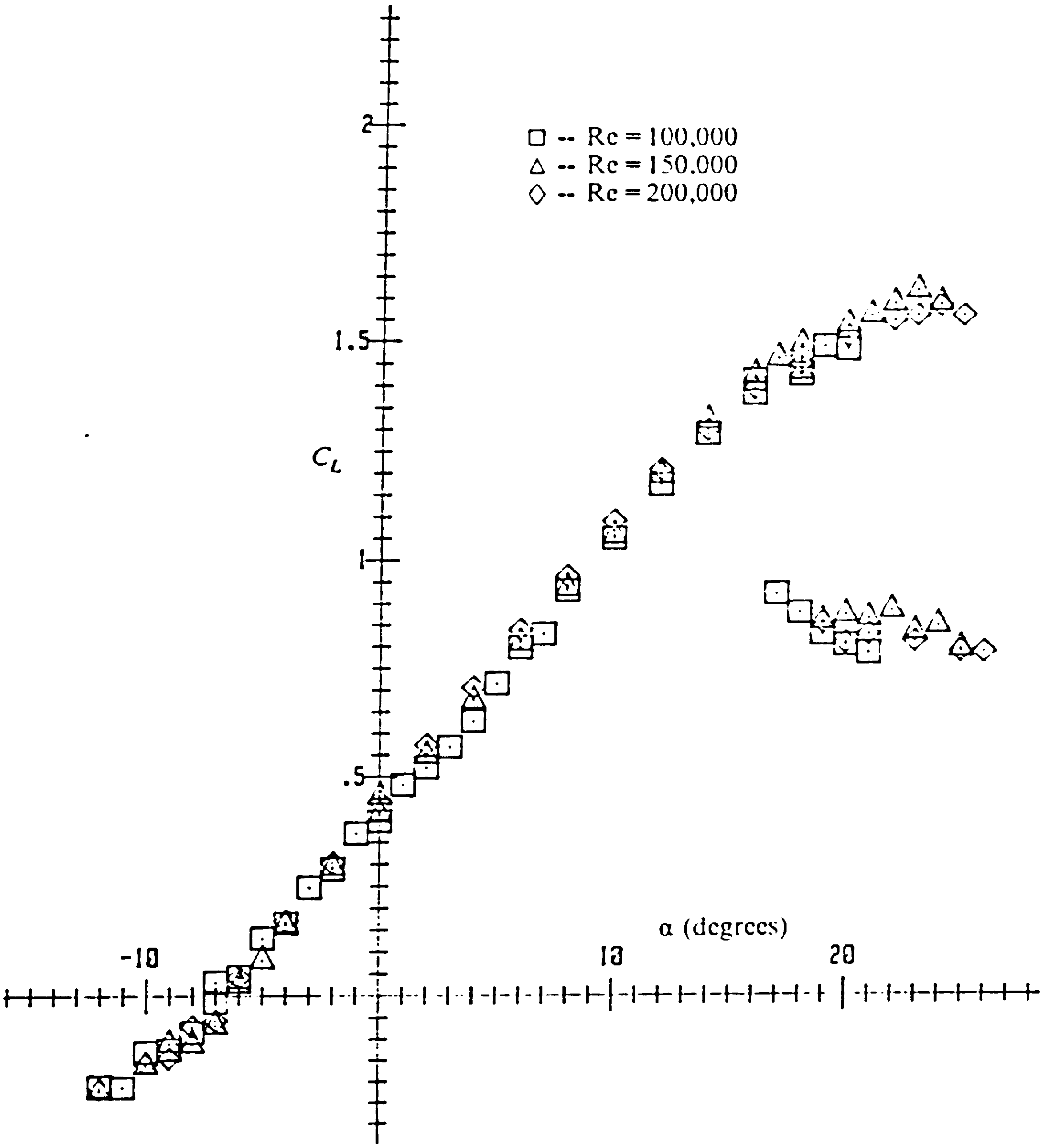

Figure 35. $C_L - \alpha$ curves for 1.5 mm. gap at different Reynolds numbers.

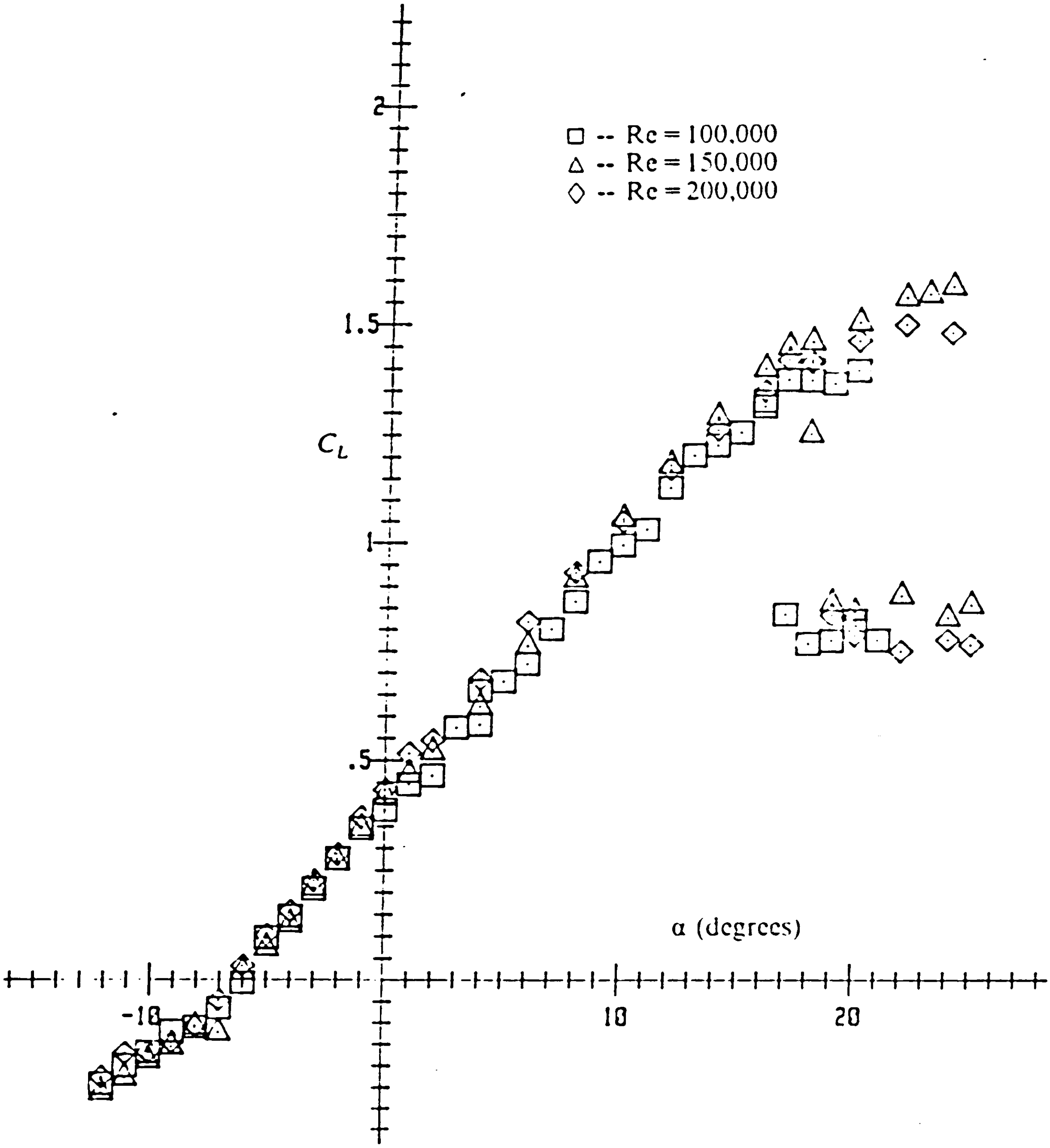

Figure 36. C_L − α curves for 2.0 mm. gap at different Reynolds numbers.

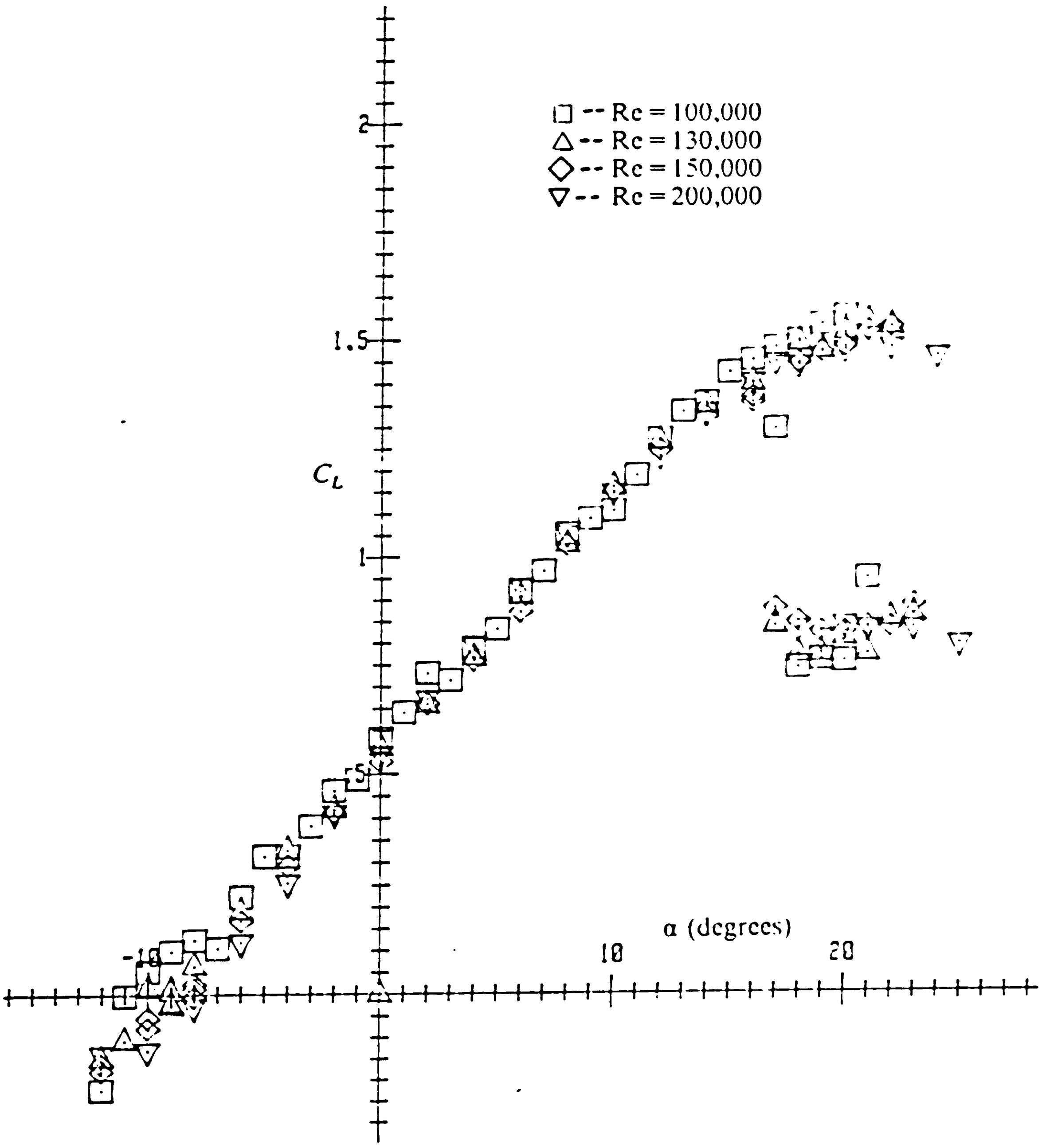

Figure 37. $C_L - \alpha$ curves for sealed gap at different Reynolds numbers.

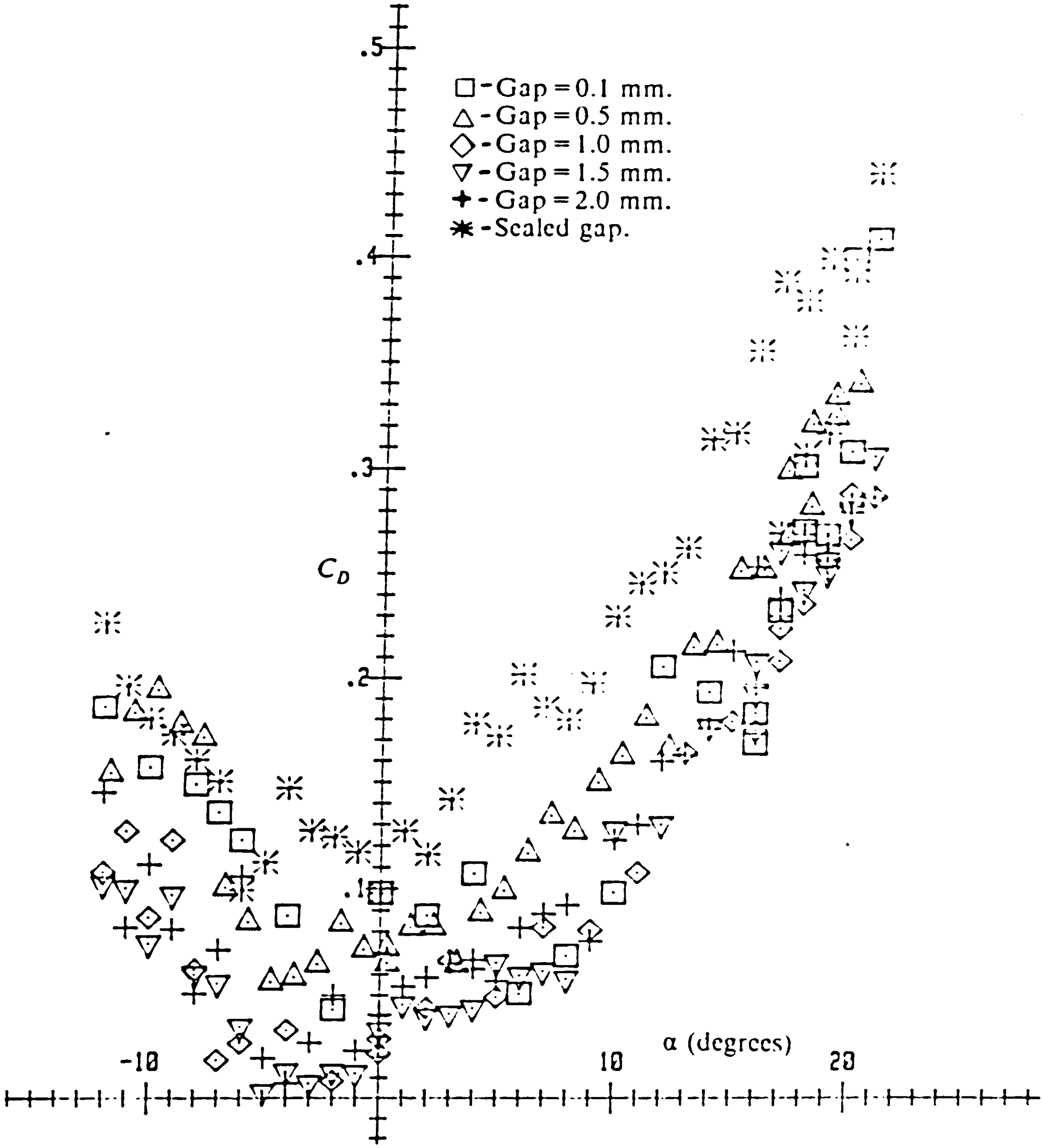

Figure 38. C_D − α curves at Re = 100,000 for different gap sizes including sealed gap.

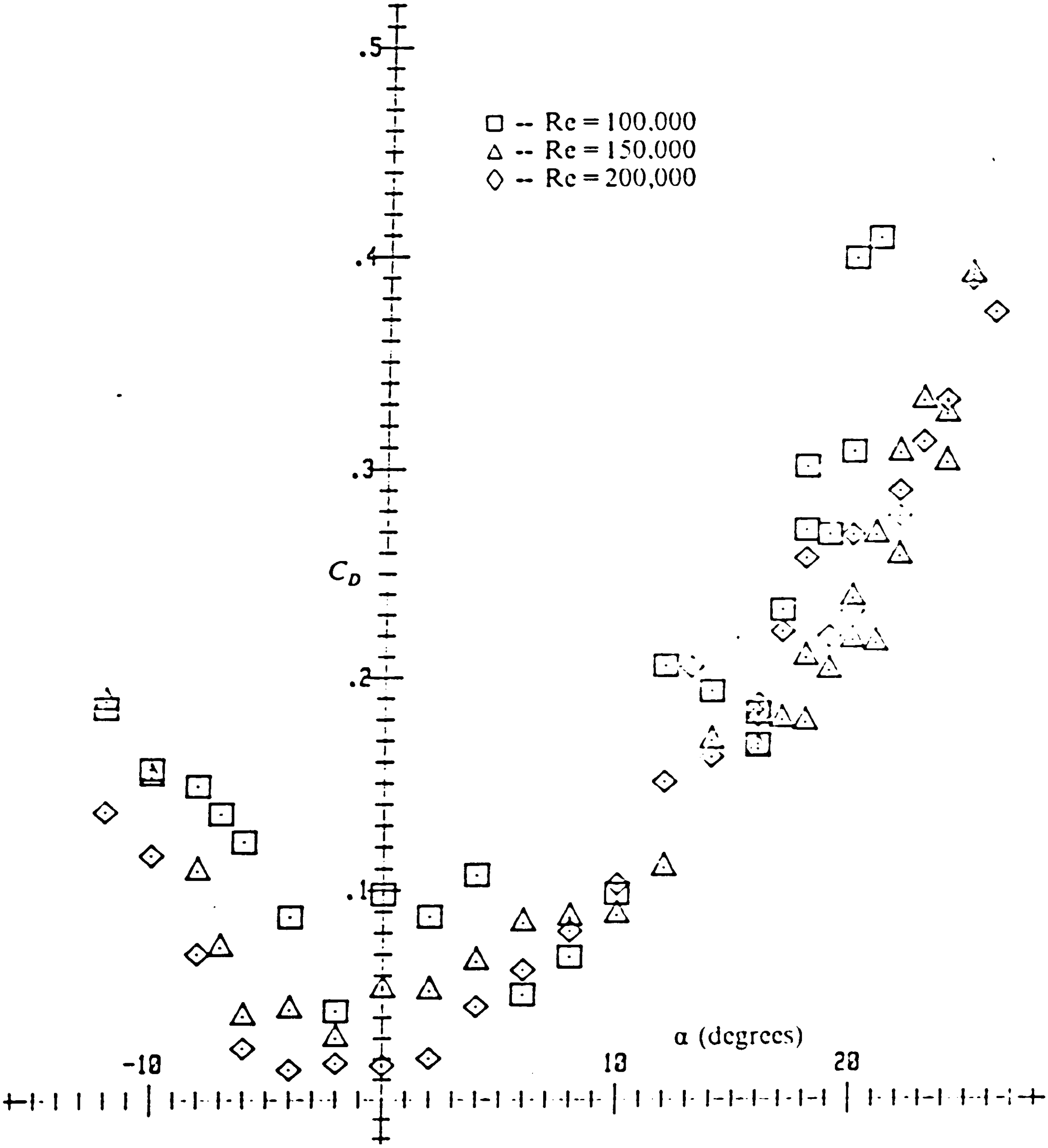

Figure 39. C_D − α curves for 0.1 mm. gap at different Reynolds numbers.

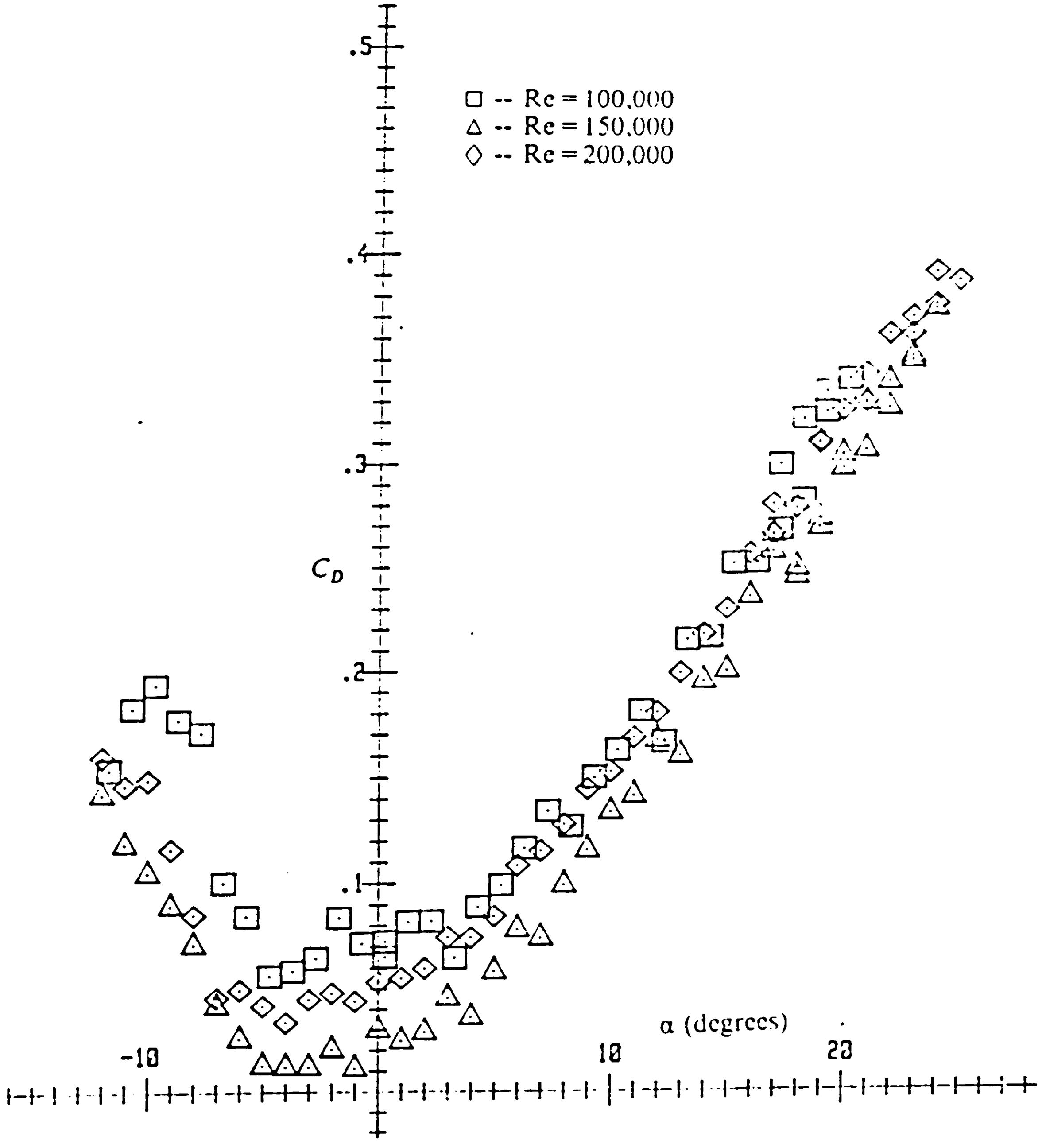

Figure 40. $C_D - \alpha$ curves for 0.5 mm. gap at different Reynolds numbers.

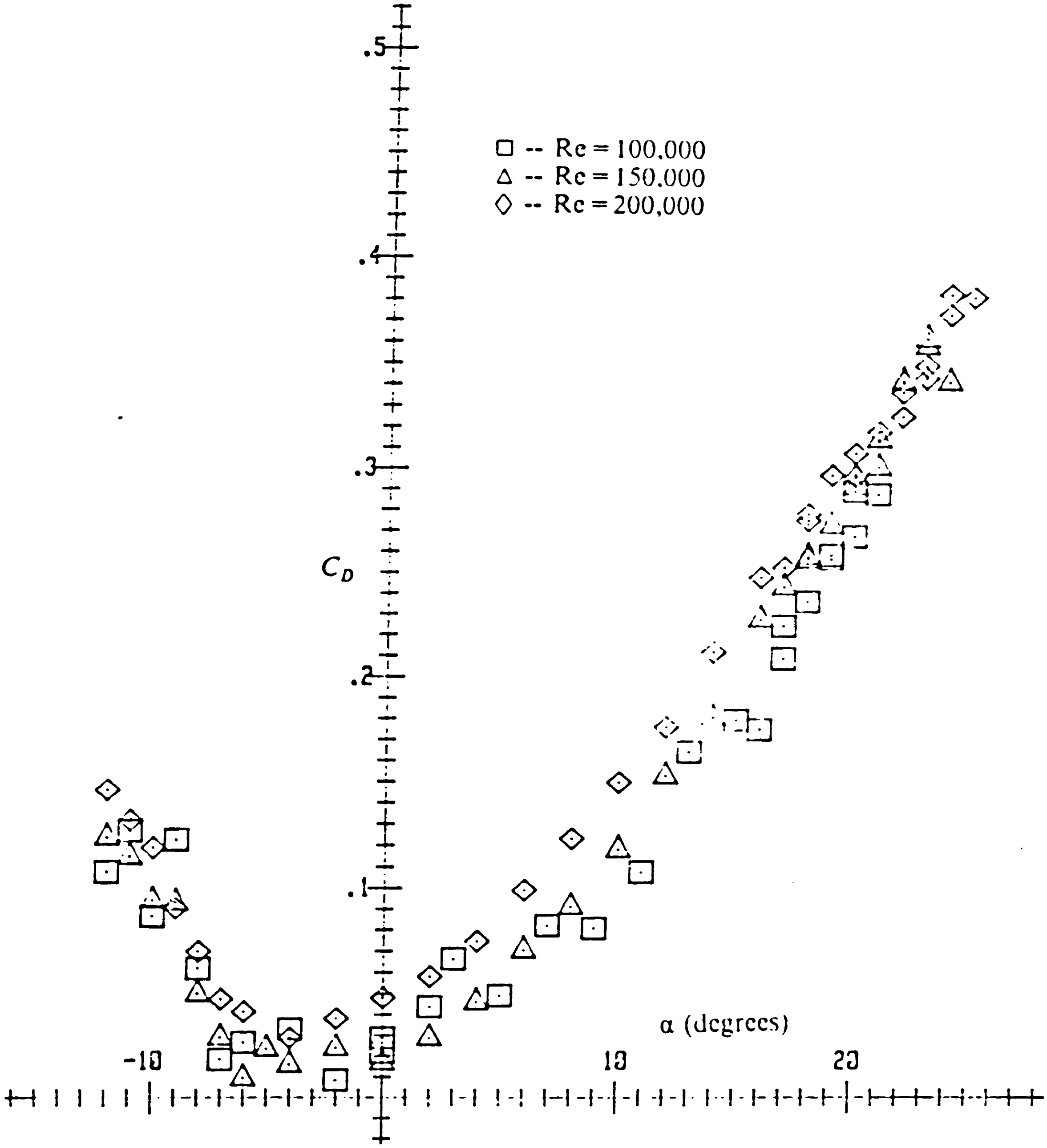

Figure 41. C_D − α curves for 1.0 mm. gap at different Reynolds numbers.

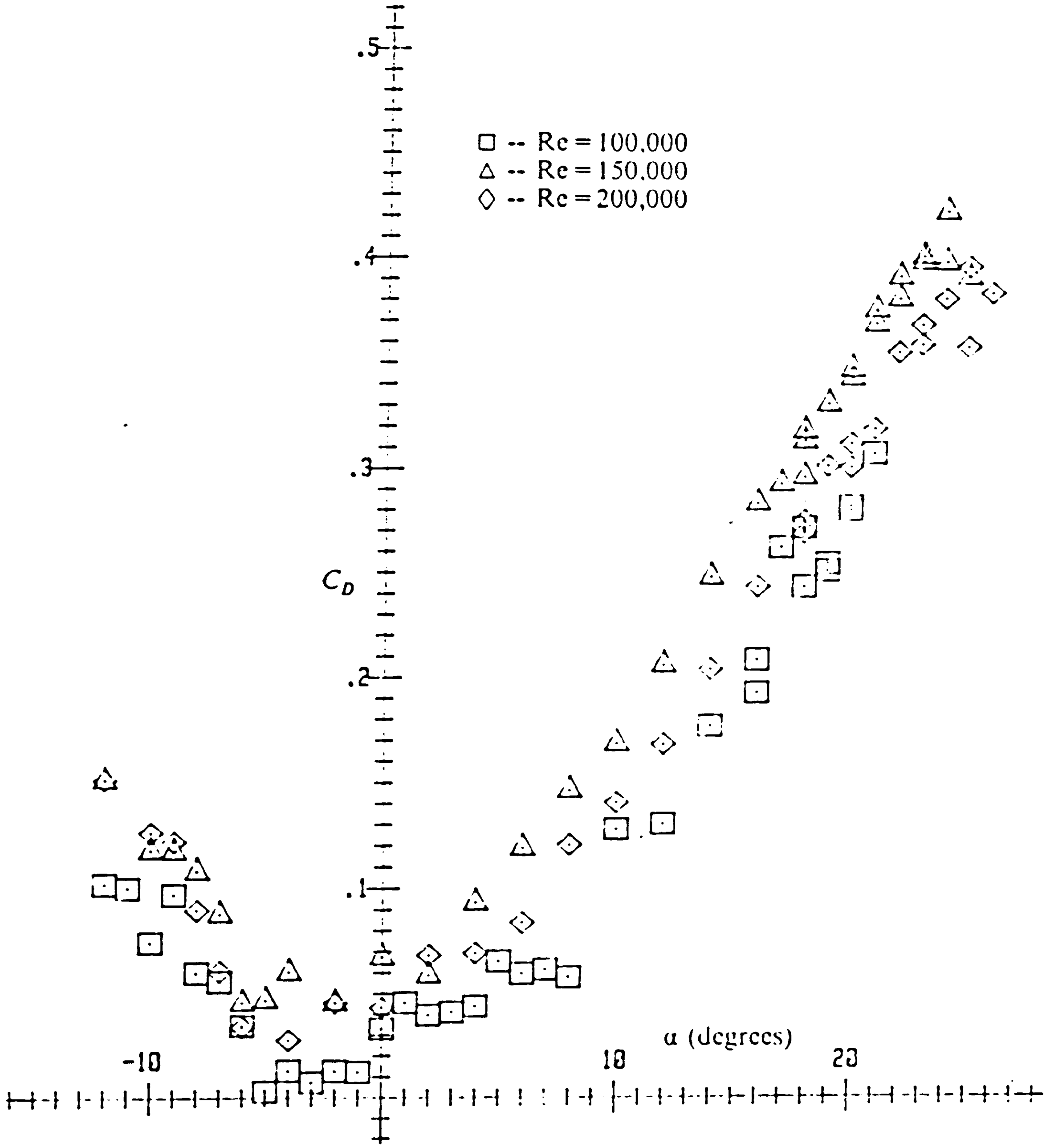

Figure 42. $C_D - \alpha$ curves for 1.5 mm. gap at different Reynolds numbers.

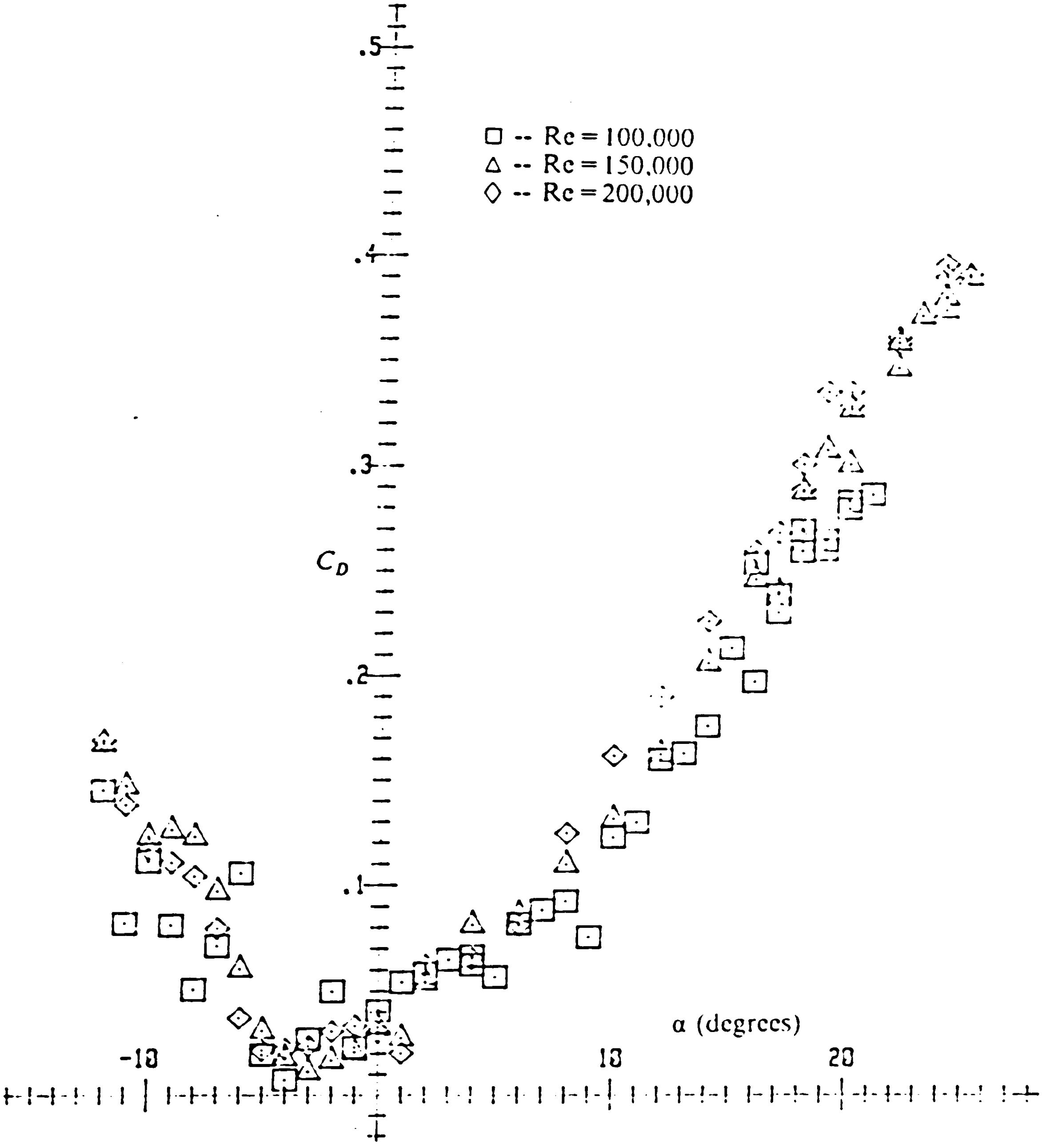

Figure 43. C_D − α curves for 2.0 mm. gap at different Reynolds numbers.

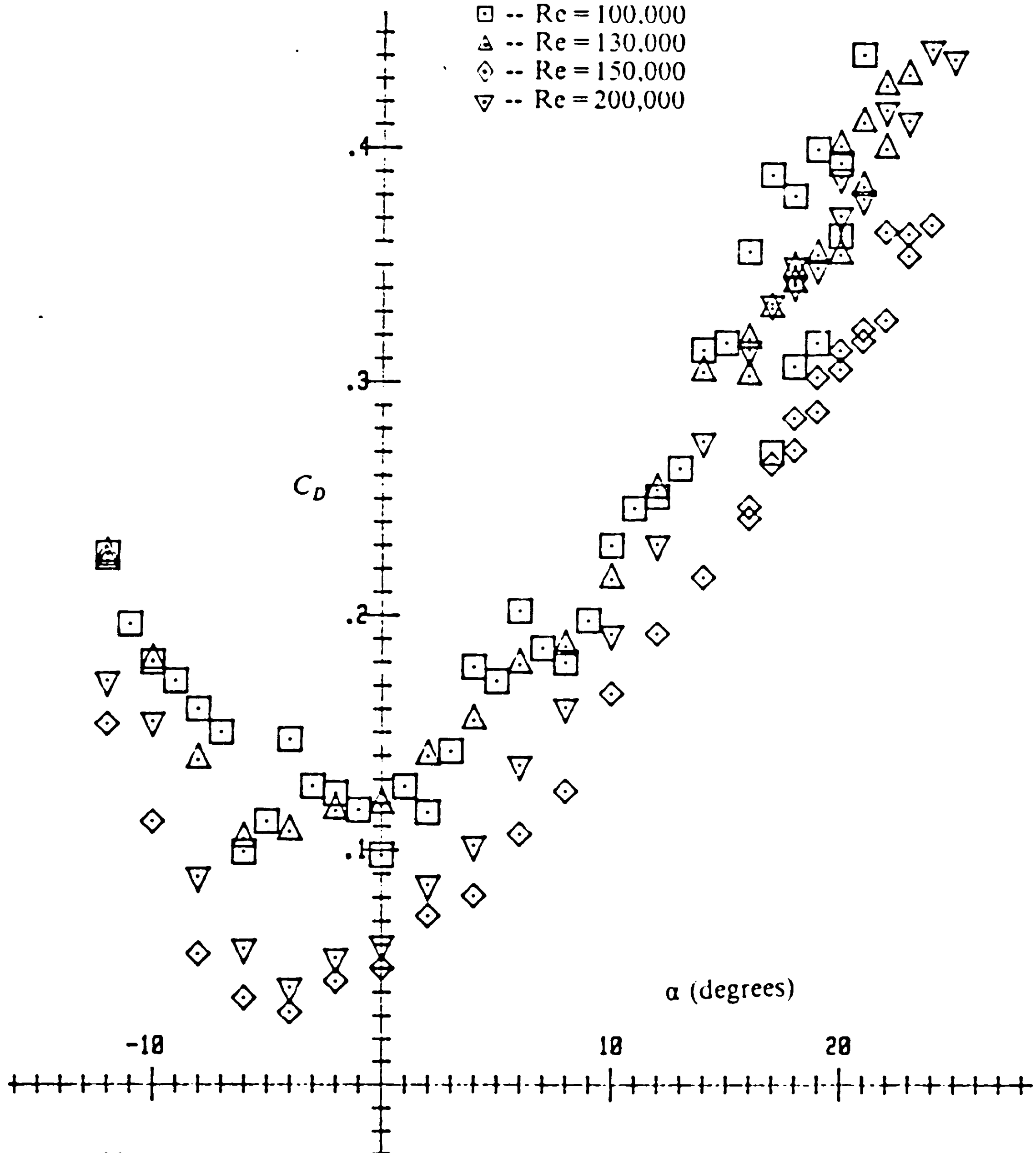

Figure 44. $C_D - \alpha$ curves for sealed gap at different Reynolds numbers.

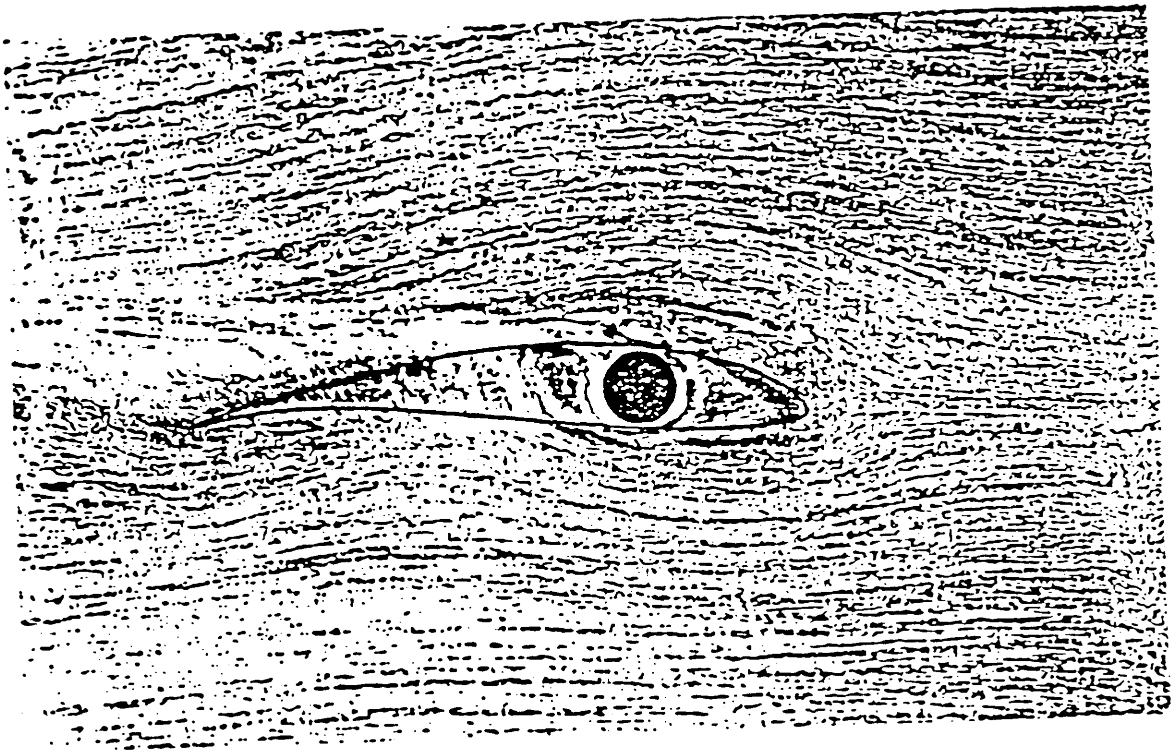

Figure 45. Surface oil flow pattern on the end plate with open gap at near zero angle incidence.

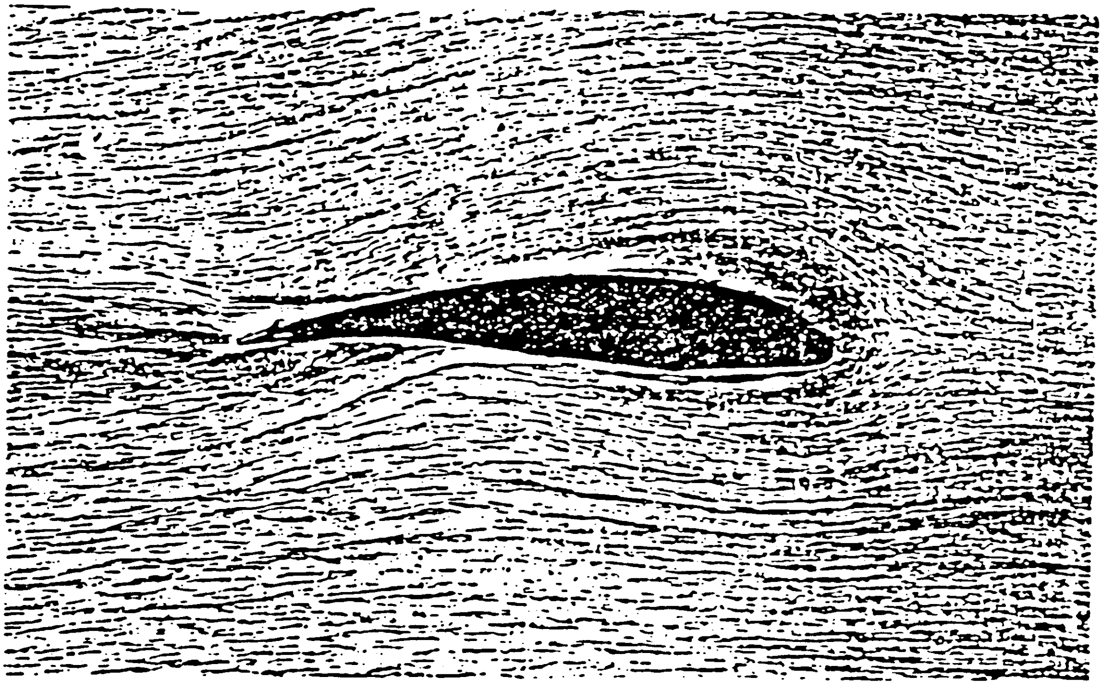

Figure 46. Surface oil flow pattern on the end plate with closed gap at near zero angle incidence.